ELSEVIER

Coastal Engineering 47 (2002) 1–26

Coastal Engineering
An International Journal for Coastal, Harbour and Offshore Engineers

www.elsevier.com/locate/coastaleng

A 2D numerical model of wave run-up and overtopping

Matthew E. Hubbard [a,*], Nick Dodd [b]

[a] School of Computing, University of Leeds, LS2 9JT Leeds, England, UK
[b] School of Civil Engineering, University of Nottingham, Nottingham, England, UK

Received 18 October 2001; received in revised form 12 June 2002; accepted 12 July 2002

Abstract

A two-dimensional (2D) numerical model of wave run-up and overtopping is presented. The model (called OTT-2D) is based on the 2D nonlinear shallow water (NLSW) equations on a sloping bed, including bed shear stress. These equations are solved using an upwind finite volume technique and a hierarchical Cartesian Adaptive Mesh Refinement (AMR) algorithm. The 2D nature of the model means that it can be used to simulate wave transformation, run-up, overtopping and regeneration by obliquely incident and multi-directional waves over alongshore-inhomogeneous sea walls and complex, submerged or surface-piercing features. The numerical technique used includes accurate shock modeling, and uses no special shoreline-tracking algorithm or shoreline coordinate transformation, which means that noncontiguous flows and multiple shorelines can easily be simulated. The adaptivity of the model ensures that only those parts of the flow that require higher resolution (such as the region of the moving shoreline) receive it, resulting in a model with a high level of efficiency. The model is shown to accurately reproduce analytical and benchmark numerical solutions. Existing wave flume and wave basin datasets are used to test the ability of the model to approximate 1D and 2D wave transformation, run-up and overtopping. Finally, we study a 2D dataset of overtopping of random waves at off-normal incidence to investigate overtopping of a sea wall by long-crested waves. The data set is interesting as it has not been studied in detail before and suggests that, in some instances, overtopping at an angle can lead to more flooding than at normal incidence.

Keywords: Run-up; Overtopping; Shallow water; Numerical models; Coastal protection; Adaptive mesh refinement

1. Introduction

Overtopping of coastal structures and inundation of coastal regions by waves is a constant hazard, the effects of which can be disastrous. A number of circumstances can contribute to such an event, including a high tide, storm surge, large waves (due to swell or wind) or a tsunami, as well as the failure of some form of sea defence, often in conjunction with the aforementioned events.

In an effort to provide guidelines for designing coastal structures that can withstand such occurrences, numerous flume and basin tests of run-up and overtopping have been performed (e.g. De Waal and Van Der Meer, 1992; Owen, 1980; Saville, 1955) and formulas and design curves for estimating maximum run-up and average overtopping rates constructed. Many of these methods are summarised in the Shore

* Corresponding author. Tel.: +44-113-343-5459; fax: +44-113-343-5468.
E-mail address: meh@comp.leeds.ac.uk (M.E. Hubbard).

0378-3839/02/$ - see front matter © 2002 Elsevier Science B.V. All rights reserved.
PII: S0378-3839(02)00094-7

Protection Manual (1984) and the Manual on the Use of Rock on Coastal and Shoreline Engineering (1991), and a review of more recent work is presented in Overtopping of Sea Walls: Design and Assessment Manual (Besley, 1999). These empirical tools have proved successful. However, they are overwhelmingly based on flume experiments with monochromatic or spectrally (and directionally) narrow-banded waves, and their application is limited to a small number of breakwater and berm types.

In recognition of these limitations, computational models have been developed (see e.g. Hibberd and Peregrine, 1979; Kobayashi and Watson, 1987; Kobayashi et al., 1987, 1989; Titov and Synolakis, 1995; Dodd, 1998; Hu et al., 2000). These are overwhelmingly based on the nonlinear shallow water (NLSW) equations, can be run at a fraction of the cost of flume tests, for any input spectrum, and are not limited by simplifications concerning the structure section or beach profile, as long as the assumptions underpinning the NLSW equations are not violated, and even in circumstances like these it has been shown (Hu et al., 2000) that the equations can give realistic predictions. They have been shown to work well in simulating wave run-up and swash motions, overtopping volumes and rates, and even regeneration of waves in the lee of a structure (see Dodd, 1998). These models are, however, all one-dimensional (1D). That is, they simulate on–offshore motions only (or in the terminology used by Titov and Synolakis, 1998, they are 1 + 1 models: one propagation direction plus time). Implicitly, therefore, they assume that a structure section or beach is alongshore-homogeneous, and that waves are shore-normal.

Fully two-dimensional (2D or 2 + 1) models of these equations and similar systems have been developed over the last 15 years. However, most of the resulting codes have been used to solve the Euler equations of gas dynamics, or to model dam-break problems or shallow water flows of hydraulics, typically without the demanding additional requirements of coastal engineering models. It is only comparatively recently that codes for coastal engineering problems have been developed. There are a number of reasons for this.

First, the calculation of the position of the time-varying shoreline has always caused problems, because of the very small depths in its vicinity. In 1D an algorithm has been developed (Hibberd and Peregrine, 1979) and refined (Kobayashi et al., 1987), which tracks the shoreline position, which is robust, but also unwieldy, and a generalisation to 2D would entail much book-keeping. A more satisfying approach (1D) was taken by Titov and Synolakis (1995) (applied to a 2D model by Titov and Synolakis, 1998), who impose a final, shoreline boundary point on the beach surface by a horizontal extrapolation of the free surface from the neighboring point (and by assuming the velocity at the shoreline node is equal to that at the neighbouring node). A simpler and more general approach was used by Watson et al. (1992), Dodd (1998), Hu et al. (2000) and Brocchini et al. (2001) (the last of these being a 2D implementation), who used Godunov-type numerical methods at all model locations. In such a treatment, the numerical fluxes are calculated by approximating a series of dam-break problems, and the shoreline becomes a special case of this, in which on one side all flow variables are zero. These methods can therefore be adapted to modeling multiple shorelines and shoreline interactions, and wave overtopping.

Second, the inevitable increase in computational expense that results from extending 1D codes to 2D can be prohibitively large. It is now becoming common for numerical models to incorporate adaptive grid techniques, or at least to use irregular grids, in recognition of this problem. Titov and Synolakis (1995) actually used an irregularly spaced grid in 1D, and reported that their model required only about half as many points per wavelength as models based on the Lax-Wendroff solver. In their 2D model, Titov and Synolakis (1998) use a finer nested grid within their main grid nearer to the shore wherever the depth falls below a certain threshold.

Finally, it is difficult to verify 2D NLSW models. This was noted by Titov and Synolakis (1998), who cited the 1D solution of Carrier and Greenspan (1958) as the only standard analytical solution (and this for strictly nonbreaking waves). Ryrie (1983) has extended this solution by assuming that the angle of propagation to the shore is small, from which assumption a new, but reduced, set of quasi-2D equations results. However, as such it is only an approximate solution to the 2D equations. The analytical solution of Thacker (1981), who considers a body of water in a parabolic bowl, is a more satisfying 2D test in that it is an exact

solution of the 2D NLSW equations (without bed friction) including a shoreline, the latter aspect being a crucial test for accurate coastal engineering codes. Furthermore, good validatory wave basin data are also difficult to find. So far, only the test of Briggs et al. (1995) looks like becoming a standard data set.

Nevertheless, in recent years 2D codes for coastal hazard problems have been developed. Titov and Synolakis (1998) give a brief description of progress to date on 2D codes, and they, Liu et al. (1995), Takahashi et al. (1995), Özkan-Haller and Kirby (1997) and Brocchini et al. (2001) have all presented and validated codes. Most of these models have primarily been developed with the modeling of tsunami run-up in mind.

Here a fully adaptive mesh approach is undertaken, in which high grid resolution is used only where necessary, thus reducing computational times, and where mesh refinement is done automatically depending on the value of a user-defined parameter, thus avoiding the necessity of choosing nested grid areas beforehand for each problem. There is no limitation to the level of refinement that can be used—other than practical ones of computational expense and memory. Furthermore, mesh refinement is achieved based not only on local depth, so that the shoreline region is well resolved, but also on local gradients in the flow, so that waves and bores are well resolved. The algorithm used is the Adaptive Mesh Refinement (AMR) algorithm of Quirk (1991) (see also Quirk and Karni, 1996). It only superimposes finer meshes over coarser ones where required, solving on all meshes but using data from the finest mesh available in each region.

In the next section, the physical and theoretical framework for the model is set out. In Section 3, the numerical model (with boundary conditions) is developed. In Section 4, a number of case studies are presented, and the model validated. In Section 5, we use OTT-2D to simulate overtopping experiments. These experiments (see Owen, 1982) are of overtopping of a sea-wall by random waves at a number of angles. They are of interest not only from the point of view of verification, but also because they show, in some cases, a peak in measured mean overtopping at oblique angles, which can seem counter-intuitive. They are therefore presented separately from the case studies of Section 4. Finally (Section 6), conclusions are arrived at.

2. Theoretical background

The physical situation is depicted in Fig. 1. The model simulates only shallow water motions, in which the fluid velocities can be assumed to be depth-uniform outside the bottom boundary layer. Accordingly, the model equations are the 2D NLSW equations, which can be written in primitive variable form as

$$\eta_t + [(h+\eta)U]_x + [(h+\eta)V]_y = 0$$

$$U_t + UU_x + VU_y + g\eta_x = -\frac{f_w}{2}\frac{|\vec{U}|\,U}{(h+\eta)}$$

$$V_t + UV_x + VV_y + g\eta_y = -\frac{f_w}{2}\frac{|\vec{U}|\,V}{(h+\eta)} \qquad (1)$$

where $U(x,y,t)$ and $V(x,y,t)$ ($\vec{U} = (U,V)$) are the water velocities in the x and y directions, $\eta(x,y,t)$ is the free surface elevation, $h(x,y)$ the still water depth, and t is the time coordinate; f_w is a dimensionless bottom friction coefficient.

Eq. (1) admits discontinuous solutions (shocks), which can evolve from continuous initial conditions,

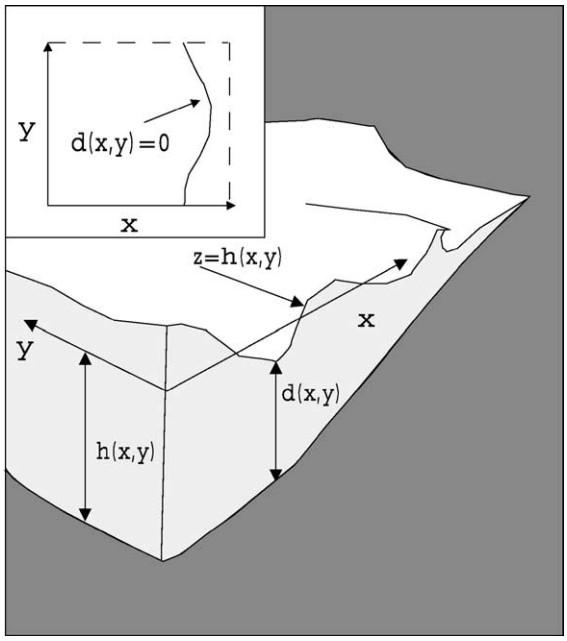

Fig. 1. A schematic depiction of the numerical wave basin. The inset gives a plan view of the model domain.

and these can be interpreted as bores, which commonly form in the inner surf zone of natural beaches, and also as waves break on steeper sea-wall slopes. Accurate modeling of these shocks is imperative in coastal engineering applications, and direct discretization of this nonconservative form of the equations will frequently lead to incorrect modelling of shock speeds.

Nondimensional coordinates are introduced: $h^*=h/h_0, \eta^*=\eta/h_0, d^*=h^*+\eta^*=d/h_0, \vec{U}^*=\vec{U}/\sqrt{gh_0}$, $x^*=x/h_0, y^*=y/h_0$ and $t^*=t\sqrt{g/h_0}$, where an asterisk denotes a nondimensional variable, and h_0 is a representative water depth, typically an average value at the offshore ($x=x_0$) boundary. The equations are then rewritten in nondimensional variables and in flux-conservative form:

$$d_t + (dU)_x + (dV)_y = 0$$

$$[dU]_t + \left[dU^2 + \frac{d^2}{2}\right]_x + [dUV]_y = dh_x - \frac{f_w}{2} U\,|\vec{U}|$$

$$[dV]_t + [dUV]_x + \left[dV^2 + \frac{d^2}{2}\right]_y = dh_y - \frac{f_w}{2} V\,|\vec{U}| \quad (2)$$

where asterisks have now been dropped for convenience. This should guarantee the correct shock speeds, as long as a conservative numerical method is applied to the fluxes.

3. Numerical model

The method used is a finite volume technique. A Cartesian mesh is used, in which the indices (i,j) represent a particular cell so, since a cell-centered scheme is used here, $d_{i,j}$ is thought of as the average depth within the cell and is nominally stored at its center. Half indices are used to represent mesh edges, the interfaces at which the fluxes are evaluated.

To illustrate the derivation of the numerical scheme, we rewrite Eq. (2) in vector form:

$$\vec{W}_t + \vec{F}_x + \vec{G}_y = \vec{S} \quad (3)$$

where

$$\vec{W} = [d, dU, dV]^T,$$

$$\vec{F} = \left[dU, dU^2 + \frac{1}{2}d^2, dUV\right]^T,$$

$$\vec{G} = \left[dV, dUV, dV^2 + \frac{1}{2}d^2\right]^T,$$

$$\vec{S} = \left[0, dh_x - \frac{f_w}{2} U\,|\vec{U}|, dh_y - \frac{f_w}{2} V\,|\vec{U}|\right]^T. \quad (4)$$

The integrated form of Eq. (3) is discretized with an explicit scheme, which applies a forward Euler discretization to the time derivative and, on a uniform grid with spacing $(\Delta x, \Delta y)$, leads to the inherently conservative method:

$$\vec{W}_{i,j}^{n+1} = \vec{W}_{i,j}^{n} - \frac{\Delta t}{\Delta x}\left(\vec{F}^*_{i+\frac{1}{2},j} - \vec{F}^*_{i-\frac{1}{2},j}\right) - \frac{\Delta t}{\Delta y}\left(\vec{G}^*_{i,j+\frac{1}{2}} - \vec{G}^*_{i,j-\frac{1}{2}}\right) + \Delta t \vec{S}^*_{i,j} \quad (5)$$

where $\vec{F}^*_{i\pm\frac{1}{2},j}$ and $\vec{G}^*_{i,j\pm\frac{1}{2}}$ are the numerical fluxes, $\vec{S}^*_{i,j}$ is the source term vector, and Δt is the time-step. The grid is depicted in Fig. 2. The flux and source terms in Eq. (5) are evaluated at time level n but the index has been dropped for brevity.

A wide variety of schemes of this form may be created by altering the construction of the numerical fluxes, $\vec{F}^*$ and $\vec{G}^*$ (and also the numerical sources $\vec{S}^*$). Here an upwind strategy is chosen, so there is no need for additional stabilisation techniques (e.g. artificial viscosity) required by central difference schemes when solution gradients are large.

3.1. Construction of fluxes

An upwind discretization can be constructed through a decomposition of the fluxes. The approximate solution is considered to be continuous within each cell (in the simplest case, which is used in this description, it is taken to be constant), but with discontinuities occurring at the cell edges, which can be represented physically as a series of Riemann problems (see e.g. Hirsch, 1990). The interface (cell-edge) fluxes are evaluated in a way designed to mimic the evolution of these sub-grid scale processes in some average sense. It is possible to solve these Riemann problems exactly (Watson et al., 1992), but it is more efficient to apply an approximate Riemann solver

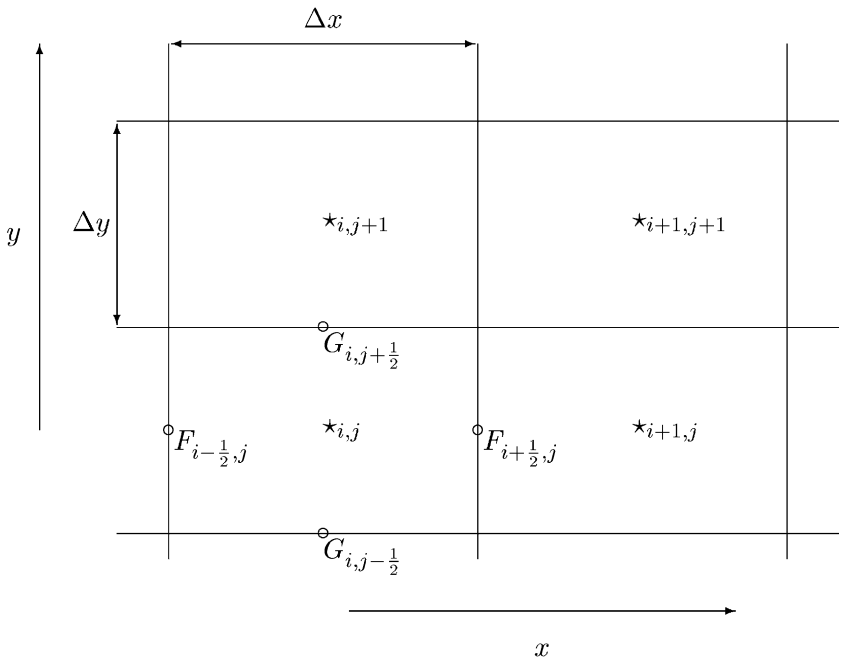

Fig. 2. The structured solution grid. ★ Indicates a cell center, at which location conserved variables are stored; ○ denotes a cell edge (interface) center, at which fluxes are evaluated.

(Dodd, 1998) (see Godunov, 1959; Harten et al., 1983; Roe, 1981; Van Leer, 1979, for the original developments in this field).

Here the approximate Riemann solver of Roe (1981) is applied to the 2D NLSW equations (e.g. Glaister, 1990; Alcrudo and Garcia-Navarro, 1993). This involves solving a locally linearised Riemann problem at each cell edge, which decouples the interface fluxes into three components, which for the NLSW equations represent a shock, a rarefaction and a shear (contact) wave, imitating the exact solution to the local Riemann problem.

This leads to a flux $\vec{F}^{*}_{i+\frac{1}{2},j}$ which is expressed as:

$$\vec{F}^{*}_{i+\frac{1}{2},j} = \frac{1}{2}(\vec{F}_{i+1,j} + \vec{F}_{i,j}) - \frac{1}{2} \times \left(\sum_{k=1}^{3} \tilde{\alpha}_k [1 - B(\tilde{r}_k)(1 - |\tilde{\nu}_k|)] |\tilde{\lambda}_k| \vec{\tilde{e}}_k \right)_{i+\frac{1}{2},j} . \quad (6)$$

Similar expressions result for $\vec{F}^{*}_{i-\frac{1}{2},j}$ and $\vec{G}^{*}_{i,j\pm\frac{1}{2}}$. Here, $\tilde{\lambda}_k$ and $\vec{\tilde{e}}_k$ are, respectively, the eigenvalues and right eigenvectors of the so-called Roe-averaged Jacobian matrix, $\tilde{A} \approx \partial\vec{F}/\partial\vec{W}$. The quantities $\tilde{\alpha}_k$ are the wave strengths. For the interface fluxes $\vec{G}^{*}_{i,j\pm\frac{1}{2}}$, analogous expressions result where $\tilde{\alpha}_k$, $\tilde{\lambda}_k$ and $\vec{\tilde{e}}_k$ relate to the matrix $\tilde{B} \approx \partial\vec{G}/\partial\vec{W}$ instead. The quantity $\tilde{\nu}_k = \tilde{\lambda}_k \Delta t/\Delta x$ is the Courant number associated with the kth wave and

$$\tilde{r}_k = \frac{\tilde{\alpha}_k^{\text{upwind}}}{\tilde{\alpha}_k^{\text{local}}} \quad (7)$$

is a ratio of wave strengths. B is a nonlinear flux limiter function, as described by LeVeque (1992). Here a number of different flux limiters are used, including *minmod*, *Van Leer*, *Van Albada* and *superbee*. Note that putting $B = 0(1)$ results in the 1st-order upwind (2nd order, Lax-Wendroff) scheme (see Hirsch, 1990; LeVeque, 1992, for more details).

Considering again the flux $\vec{F}^{*}_{i+\frac{1}{2},j}$, expressions for each of the quantities in Eq. (6) are:

$$\tilde{\alpha}_1 = \frac{\Delta(d)}{2} + \frac{1}{2\tilde{c}}[\Delta(dU) - \Delta(d)\tilde{U}]$$

$$\tilde{\alpha}_2 = \frac{1}{\tilde{c}}[\Delta(dV) - \Delta(d)\tilde{V}]$$

$$\tilde{\alpha}_3 = \frac{\Delta(d)}{2} - \frac{1}{2\tilde{c}}[\Delta(dU) - \Delta(d)\tilde{U}]$$

$$\tilde{\lambda}_1 = \tilde{U} + \tilde{c}$$

$$\tilde{\lambda}_2 = \tilde{U}$$

$$\tilde{\lambda}_3 = \tilde{U} - \tilde{c}$$

$$\vec{\tilde{e}}_1 = [1, \tilde{U} + \tilde{c}, \tilde{V}]^T$$

$$\vec{\tilde{e}}_2 = [0, 0, \tilde{c}]^T$$

$$\vec{\tilde{e}}_3 = [1, \tilde{U} - \tilde{c}, \tilde{V}]^T \tag{8}$$

in which the Roe-averaged quantities (indicated by $\tilde{\cdot}$) are given by

$$\tilde{c} = \sqrt{\frac{d_R + d_L}{2}}$$

$$\tilde{U} = \frac{U_R\sqrt{d_R} + U_L\sqrt{d_L}}{\sqrt{d_R} + \sqrt{d_L}}$$

$$\tilde{V} = \frac{V_R\sqrt{d_R} + V_L\sqrt{d_L}}{\sqrt{d_R} + \sqrt{d_L}} \tag{9}$$

The subscripts R and L refer to "Right" and "Left" states in the sub-grid dam-break problem (in this case with respect to the x direction), and quantities $\Delta(\cdot)$ represent the difference between the two states. The corresponding expressions for the flux in the y-direction, $\vec{G}^*_{i,j+\frac{1}{2}}$, are

$$\tilde{\alpha}_1 = \frac{\Delta(d)}{2} + \frac{1}{2\tilde{c}}[\Delta(dV) - \Delta(d)\tilde{V}]$$

$$\tilde{\alpha}_2 = \frac{1}{\tilde{c}}[-\Delta(dU) + \Delta(d)\tilde{U}]$$

$$\tilde{\alpha}_3 = \frac{\Delta(d)}{2} - \frac{1}{2\tilde{c}}[\Delta(dV) - \Delta(d)\tilde{V}]$$

$$\tilde{\lambda}_1 = \tilde{V} + \tilde{c}$$

$$\tilde{\lambda}_2 = \tilde{V}$$

$$\tilde{\lambda}_3 = \tilde{V} - \tilde{c}$$

$$\vec{\tilde{e}}_1 = [1, \tilde{U}, \tilde{V} + \tilde{c}]^T$$

$$\vec{\tilde{e}}_2 = [0, -\tilde{c}, 0]^T$$

$$\vec{\tilde{e}}_3 = [1, \tilde{U}, \tilde{V} - \tilde{c}]^T. \tag{10}$$

As it stands, the scheme allows nonphysical numerical solutions (expansion shocks). These can be avoided by applying a numerical device (entropy fix), which ensures that the approximate solution satisfies an entropy condition. The approach of Roe (1985) is used here. Along with this entropy fix, the numerical scheme used comprises Eq. (5) with interface fluxes given by Eq. (6) and their counterparts. See Hirsch (1990), LeVeque (1992) and Toro (1997) for fuller explanations of these methods; see Alcrudo and Garcia-Navarro (1993) or Hubbard (1999) for further details relating to their application to the nonlinear shallow water equations.

The time-step is restricted for stability purposes so that no wave resulting at an interface can travel beyond the extent of its stencil. This leads to the constraint

$$\Delta_t \leq \frac{\min(\Delta x, \Delta y)}{2\max_{i,j}(|\vec{U}_{i,j}| + c_{i,j})}, \tag{11}$$

where $c = \sqrt{d}$ is the (nondimensional) gravity wave speed, and the maximum is taken over every cell of the mesh. Throughout this work, a time-step of $0.8\Delta t_{max}$ has been used, ensuring the robustness of the calculations.

3.2. Source terms

The discretization of the bed slope source terms differs substantially from the usual methods, very few of which take account of the form of the flux discretization. The appropriate component of $\vec{S}^*_{i,j}$ in Eq. (5) is calculated so that equilibria maintained by the original equation (Eq. (2)) are also satisfied by the numerical approximation. To this end the source terms are decomposed into characteristic components, similar to the flux difference.

The complete discretization of the source term associated with cell (i,j) is then

$$\vec{S}^{*}_{i,j} = \vec{S}^{-}_{i+\frac{1}{2},j} + \vec{S}^{+}_{i-\frac{1}{2},j} + \vec{S}^{-}_{i,j+\frac{1}{2}} + \vec{S}^{+}_{i,j-\frac{1}{2}} \tag{12}$$

where, in order to obtain the correct balance with the limited higher order fluxes defined in Eq. (6), the four interface source terms above can be constructed from

$$\vec{S}^{\pm} = \frac{1}{2}\sum_{k=1}^{3}(1 \pm \mathrm{sign}(\tilde{\lambda}_k)[1 - B(\tilde{r}_k)(1 - |\tilde{v}_k|)])\tilde{\beta}_k \vec{\tilde{e}}_k, \tag{13}$$

(with the inclusion of appropriate edge subscripts) in which $\tilde{\beta}_k$ are the coefficients of the decomposition of the source term onto the eigenvectors $\vec{\tilde{e}}_k$ of the appropriate flux Jacobians. Details can be found in Hubbard and Garcia-Navarro (2000). The bed friction source terms are evaluated pointwise, i.e. $\vec{S}^{*}_{i,j} = \vec{S}(\vec{W}_{i,j})$.

3.3. Adaptive mesh refinement

We use the AMR algorithm of Quirk (1991). The method is based on the earlier work of Berger and Oliger (1984) and Berger and Colella (1989).

The method uses a hierarchical system of grids, the coarsest, denoted G_0 (see Fig. 3), consists of a single mesh, the term 'mesh' being used to define a single rectangular patch of cells. Each of the finer grid levels (G_1, G_2, etc.) may consist of any number of meshes. Here the fine meshes are constructed so as to lie completely within a single mesh at the coarser level and no two meshes within the same grid are allowed to overlap. The relative level of refinement between two grid levels can take any positive integer value and need not be the same in each coordinate direction. This allows a high degree of pre-tuning to the problem in hand, if so wished.

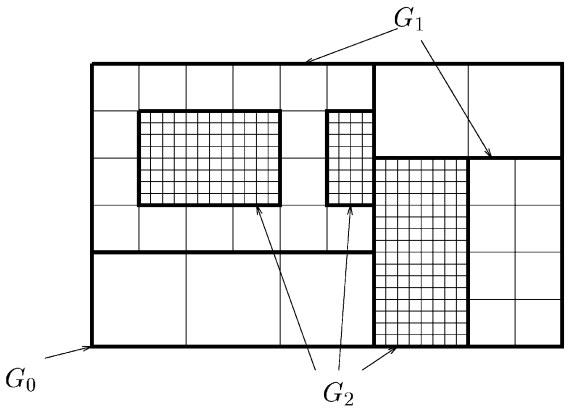

Fig. 3. An example of an adapted grid.

Information is continually passed both ways between the different grid levels via layers of dummy cells surrounding each mesh, and the grids themselves are refined and derefined regularly so that flow features of interest are followed by regions of high grid resolution and the algorithm is genuinely time dependent. Furthermore, an adaptive time-stepping strategy is used, which avoids unnecessarily prohibitive restrictions on the time-step used in the integration of the equations on the coarser grids.

3.3.1. Flagging for refinement

The adaptation step is designed to ensure that the fine meshes (which give the high grid resolution) follow the movement of the flow features they are intended to resolve. Here the monitor function is

$$\xi_{i,j} = \max_{l=1,N_c} \frac{|d_{i,j} - d_l|}{\min(d_{i,j}, d_l)}, \tag{14}$$

where N_c is the number of adjacent cells, and relates the depth of water in cell (i,j) to that in its neighbors. This monitor is sensitive to the gradient of the depth relative to the depth itself and advocates refinement both in regions where the depth is changing rapidly (e.g. in bores) and in cells close to the moving shoreline where the water is very shallow.

During adaptation, mesh cells are flagged for refinement when $\xi_{i,j}$ exceeds a critical, specified value: ξ_{crit}. The flagged cells are "clustered" into new rectangular meshes that are constructed so as to completely cover the flagged region, subject to a specified tolerance (T) that dictates the proportion of unflagged cells allowed in the new meshes. Setting $T=1$ ensures that the new meshes contain only flagged cells; $T=0$ creates a single mesh that constitutes the smallest rectangle covering the flagged cells. The value of T is chosen to provide a balance between creating many small meshes (with the consequent communication overhead between them) and few large meshes (which contain a large proportion of redundantly refined cells) and typically takes a value of

between 0.6 and 0.8. A value of 0.8 is used throughout this work.

3.4. Boundary conditions

3.4.1. Internal boundary conditions

Each mesh is surrounded by a double layer of dummy cells which, prior to each grid integration, are primed with information about the solution around the boundary of the mesh. This allows the mesh boundaries to be invisible to the mesh integrator being used since no special treatment is required beyond the overwriting of the solution in the dummy cells. Most of these mesh boundaries lie within the computational domain, in which case the solution in the dummy cells is taken from the finest mesh underlying those cells (see Quirk, 1991). When the mesh boundaries coincide with domain boundaries the dummy cells are supplied with information appropriate to the specified external boundary type.

3.4.2. External boundaries

It is also possible to use the dummy cell approach to model simple external boundary conditions. The four types of boundary used here are *extrapolation* (dummy cells are overwritten with the solution values in the cells along the boundary, giving a very simple absorbing boundary suitable for outflow); *reflection* (the normal velocity components of the flow in the dummy cells are taken to be a reflection in the domain boundary of the internal values, imitating a solid wall); *periodic* (the solution at one end of the domain provides an input boundary at the opposite edge); and a simple *absorbing/generating boundary* (the solution in the dummy cells at an offshore boundary is interpolated linearly from a time series of data, either synthetic or measured).

3.4.3. The shoreline

No special tracking procedure has been used here; instead, a distinction is made between wet cells and dry cells (in which the depth of water is less than a specified tolerance d_{tol}) and the shoreline is constructed from the mesh interfaces between wet and dry cells (i.e. there is no interpolation).

The detailed wetting/drying procedure used is similar to that of Sleigh et al. (1998) and the adaptation monitor (Eq. (14)) is chosen so that the shoreline region is covered with the finest possible mesh and the simple modeling procedure used at the shoreline does not inhibit the overall accuracy of the solution.

At the beginning of each mesh integration, a cell wetting procedure is carried out. The mesh is searched for dry cells ($d < d_{\mathrm{tol}}$) which are in imminent danger of flooding, i.e. the bed of the cell is below the water level in one or more of its neighbors, as illustrated by the 'wet' cell and its right-hand neighbor in Fig. 4. Each cell with this property is then wetted by setting $d = d_{\mathrm{tol}}$ (and keeping $U = V = 0$), which gives it a prespecified small water depth. This enables Roe's scheme to be used without alteration when calculating the interface fluxes in this cell.

The mesh integrator then calculates fluxes at three different types of internal edge, which are treated as follows:

- *wet/wet*—use Roe's scheme as normal for both cells.
- *dry/dry*—ignore completely, no contribution is made to either cell.
- *wet/dry*—no update is made to either cell from this edge. This is done because it has already been decided that the dry cell will remain dry, so a zero flux condition is applied to this edge. This mimics a solid wall boundary so it allows the definition of the bathymetry to create solid wall boundaries within the domain by setting a value of h which will never be inundated.

An example of each type of interface is shown in Fig. 4.

Having completed the update, the depth of water in some cells may have dropped below d_{tol}. These cells are considered to be dry and their depth d is reset to zero. Note that this will automatically allow for the emergence of bed features which were initially completely submerged. Furthermore, in cells where the

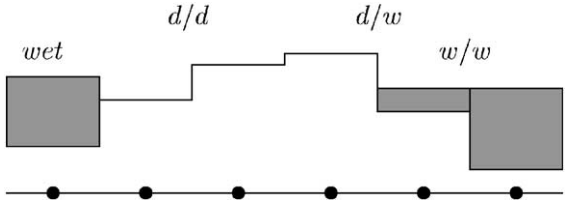

Fig. 4. The wetting/drying procedure illustrated in 1D. Solid circles indicate cell centers.

depth is very small the local velocity may be very high since these are calculated from the approximations to dU and dV. This unnecessarily restricts the global time-step. This difficulty is overcome by introducing a second depth tolerance $d_{TOL}>d_{tol}$ (see Sleigh et al., 1998), which defines cells that are 'almost dry'. When the depth of water in a cell drops below d_{TOL} the depth is not altered but the x and y momentum (dU and dV) is set to zero. This stabilises the scheme in the vicinity of the shoreline with negligible effect on the global solution. Throughout this study we set $d_{TOL}=10\times d_{tol}$.

Lastly, for output purposes a further parameter d_{shore} is defined, which defines the shoreline, and is equivalent to the distance above a beach of a wave gage. It has no effect on the numerical solution scheme.

4. Case studies

Validation of the model is split into five phases: (1) verification against a 1D analytical solution of run-up of nonbreaking waves; (2) testing against 1D (flume) data sets of overtopping by random waves; (3) validation against a genuinely 2D analytical solution of the model equations; (4) application to 2D run-up of nonbreaking waves and comparison with another 2D numerical solution for the same case; and (5) testing against 2D (wave basin) data sets of breaking tsunami wave run-up around a circular island, and qualitative comparison against other numerical solutions for the same case.

These five cases present an exhaustive validation of the numerical model as compared against analytical solutions of the NLSW equations, results obtained by approximating more complicated applications of the NLSW equations using competing numerical models, and experimental results.

4.1. 1D validation

We test the model against the 1D solution of Carrier and Greenspan (1958). The analytical solution tested here is for the run-up and run-down of periodic nonbreaking waves on a constant sloping beach. Details of the solution, which is obtained via a hodograph transformation of the NLSW equations, can be found in Carrier and Greenspan (1958). One way of representing the solution (in nondimensional form) is through a nondimensional amplitude A (see Brocchini and Peregrine, 1996), which is related to the dimensional run-up amplitude, wave period and beach slope. For nonbreaking waves $A\leq 1$ (see Brocchini et al., 2001, for a comparison with the quasi-2D solution of Brocchini and Peregrine, 1996).

Two cases are tested here: $A=0.5$ and $A=1.0$. The OTT-2D runs were done with $f_w=0$ for consistency with the analytical solution, depth tolerances of $d_{tol}=0.0001$ m and $d_{shore}=0.001$ m, and a critical refinement factor (Eq. (14)) of $\xi_{crit}=0.01$. The *minmod* flux limiter was used, on a coarse grid of 192 cells with two levels of refinement, both by a factor of 2. The cross-shore profiles of η and U are both in extremely good agreement with the exact solution, being almost indistinguishable when visualised except for small discrepancies at the shoreline. The velocities, which are particularly difficult to model accurately, are shown in Fig. 5. The exact and numerical shoreline positions are compared through a single wave period in Fig. 6. Careful inspection shows that the comparison is good for both the fine grid approximation and the adaptive approximation with equivalent fine grid resolution.

4.2. 1D datasets

Dodd (1998) presented a comparison between mean overtopping rates measured during a series of random wave tests and the equivalent predictions made by a 1D model (OTT). The 2D model presented here is similarly verified against both measured and (1D) predicted rates. The overtopping tests consisted of flume tests in which JONSWAP spectra waves were generated at the paddle, on water depths of 0.7 and 0.6 m. The waves were subsequently transformed on a 1:50 approach slope (total length 20 m), and finally encountered a sea wall of slope 1:4. More details of the tests are given in Dodd (1998) and Coates et al. (1998). Overtopping rates were then calculated based on 1000 mean wave periods, or until the overtopping tank filled up.

In the present numerical tests, OTT-2D was run for the 14 tests presented in Table 3 of Dodd (1998). The present model was run with $d_{tol}=0.003$ m for consistency with OTT (see Table 4 of Dodd, 1998) and an identical friction coefficient: $f_w=0.02$. The model was

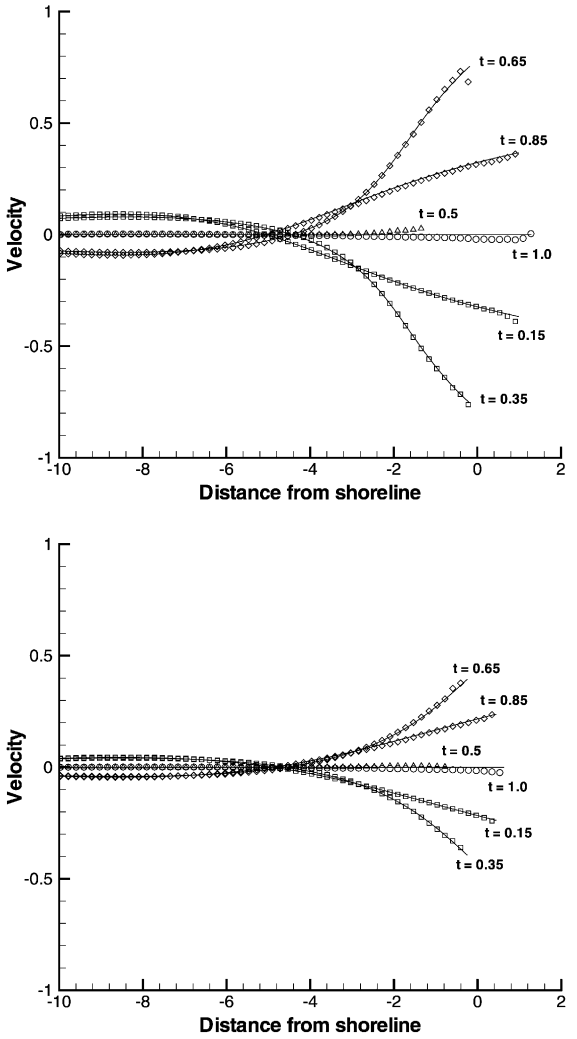

Fig. 5. Velocities (U) at nondimensional times 0.15, 0.35, 0.5, 0.65, 0.85 and 1.0 (the last being a full wave period) for dimensionless shoreline amplitudes of $A=1.0$ (top) and $A=0.5$ (bottom) of the nonbreaking Carrier and Greenspan wave. The solid lines represent the exact solution while the symbols represent the solution obtained using the current scheme on a grid of 192 cells with two levels of refinement, each by a factor of 2.

run in nonadaptive grid mode, with the same number of computational cells and offshore boundary conditions as OTT, in order to make conditions as close as possible to the former tests.

The results are shown in Table 1. There is a clear tendency for OTT-2D to underpredict compared to OTT in most tests, sometimes significantly. This discrepancy sometimes results in closer agreement with measurement (tests 0e47 and 0f47) and sometimes not (tests 0g47, 0d27 and 0f27). It is not clear what the discrepancy is due to, although it might be due to a slightly different shoreline treatment (both its definition and the wet/dry interface treatment) and/or source term discretization. For engineering purposes, however, results are satisfactory, and OTT-2D can be re-calibrated by altering the value of f_w.

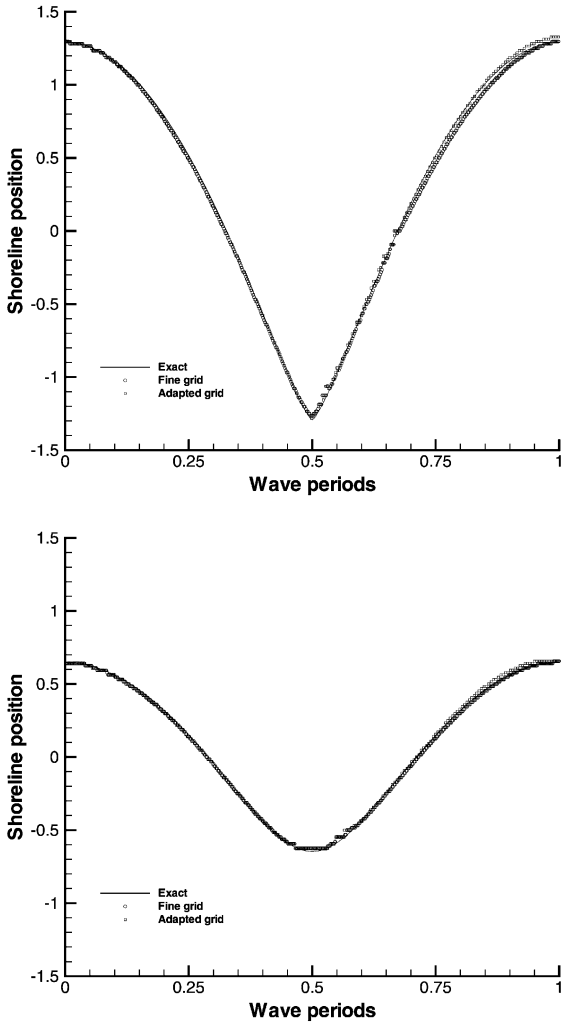

Fig. 6. The shoreline position over one wave period for dimensionless shoreline amplitudes of $A=1.0$ (top) and $A=0.5$ (bottom) of the nonbreaking Carrier and Greenspan wave. The solid lines represent the exact solution while the symbols represent the solutions obtained using the current scheme on a grid of 192 cells with two levels of refinement, each by a factor of 2 (squares), and a single, equivalent resolution grid of 768 cells (circles).

Table 1
Wave conditions for the JONSWAP spectrum random wave flume tests detailed in Dodd (1998) and Coates et al. (1998)

Test	H_s (m)	T_m (s)	SWD (m) at Paddle	Q (l s^{-1} m^{-1})		
				Measured	OTT	OTT-2D
0b27	2.0	8.01	14.0	19	13	13
0b47	2.12	6.08	14.0	6	2	1
0c46	2.5	6.31	12.0	1	0	0
0c47	2.5	6.31	14.0	20	6	4
0d26	2.76	10.02	12.0	13	15	5
0d46	3.0	6.89	12.0	2	1	0
0e47	3.5	7.51	14.0	115	154	127
0f26	4.0	11.31	12.0	21	14	12
0f46	4.0	8.01	12.0	5	3	3
0f47	4.0	8.01	14.0	181	233	191
0g47	4.5	8.50	14.0	273	261	196
0d27	2.76	10.02	14.0	177	171	131
0f27	4.0	11.31	14.0	363	369	309

Also shown are the mean overtopping rates associated with these tests: measured, predicted by OTT (see Dodd, 1998), and predicted by OTT-2D. Nonadaptive grid used with *superbee* flux limiter, $f_w = 0.02$, $d_{tol} = 0.003$ m and $N = 100$. All quantities are to prototype scale.

4.3. 2D validation

The 2D analytical solution of the NLSW equations compared with here is due to Thacker (1981). This paper contains a family of periodic solutions based on parabolic circular and elliptic bowl geometries, which should be of great interest to the coastal engineering community. They model a variety of situations, such as flood waves and wave run-up and run-down (both normal and oblique to the shoreline). The test case chosen here is the most difficult for the numerical model because it involves both wetting and drying of surfaces (unlike the parabolic flood wave, which is also modelled extremely well by this method) and is not radially symmetric (the sample solutions given are also similar in nature to the 1D Carrier–Greenspan test case presented earlier).

The flow takes place inside a parabola of revolution, given by

$$h = h_0\left(1 - \frac{x^2 + y^2}{L^2}\right), \tag{15}$$

which leads to an exact, periodic, solution of the NLSW equations of the form

$$\eta = \frac{\eta h_0}{L^2}\left(2x\cos\omega t + 2y\sin\omega t - \eta\right)$$

$$u = -v\omega\sin\omega t$$

$$v = -v\omega\cos\omega t \tag{16}$$

where $\omega = \sqrt{2gh_0}/L$. The free parameters are chosen here to be $h_0 = 0.1$, $L = 1.0$ and $\eta = 0.5$ and the solution when $t = 0$ is supplied as initial conditions. Unlike the Carrier–Greenspan solution, this is not driven by external boundary conditions. This exact solution simulates a circle of water with a free surface of constant gradient at any given instant travelling in a circle around the centre of the bowl with constant angular velocity and without changing shape. The solution is thus periodic and should return to its initial conditions after any integer number of periods.

The numerical results obtained on the domain $[-2,2] \times [-2,2]$ using a 40×40 cell coarse grid with three levels of refinement (by a factor of 2 in each direction at each level) are shown in Fig. 7. A small distortion is seen in the circular depth profile after a single period, but the slice through the centre shows that the difference is not that great. Far more difficult to model accurately is the velocity, but the same figure shows that this is also done well, with the largest differences being on the periphery, close to where the moving shoreline is being modelled and where the depth of the water is almost zero.

4.4. 2D numerical comparison

One test of shallow water motions in 2D that has been used previously is that first performed by Zelt (1986). In this test, a solitary wave runs up on a bay with a sloping bottom. The bathymetry is shown in Fig. 8. There is no analytical solution for this case, but other shallow water codes have been tested against the Lagrangian model of Zelt. Here we test the present code against another NLSW equation solver (Özkan-Haller and Kirby, 1997). Following Özkan-Haller and Kirby (1997), we define the bathymetry as:

$$h = \begin{cases} h_0 - h_0\left\{\frac{x - 3L/\pi}{\zeta_0(y) - 3L/\pi}\right\} & \text{for } x \le \frac{3L}{\pi} \\ h_0 & \text{for } x > \frac{3L}{\pi} \end{cases} \tag{17}$$

where $\zeta_0(y) = -\frac{L}{\pi}\cos\frac{\pi y}{L}$, so that L is the half-width of the bay and h_0 is the offshore (constant) depth. The solitary wave profile is defined in Özkan-Haller and

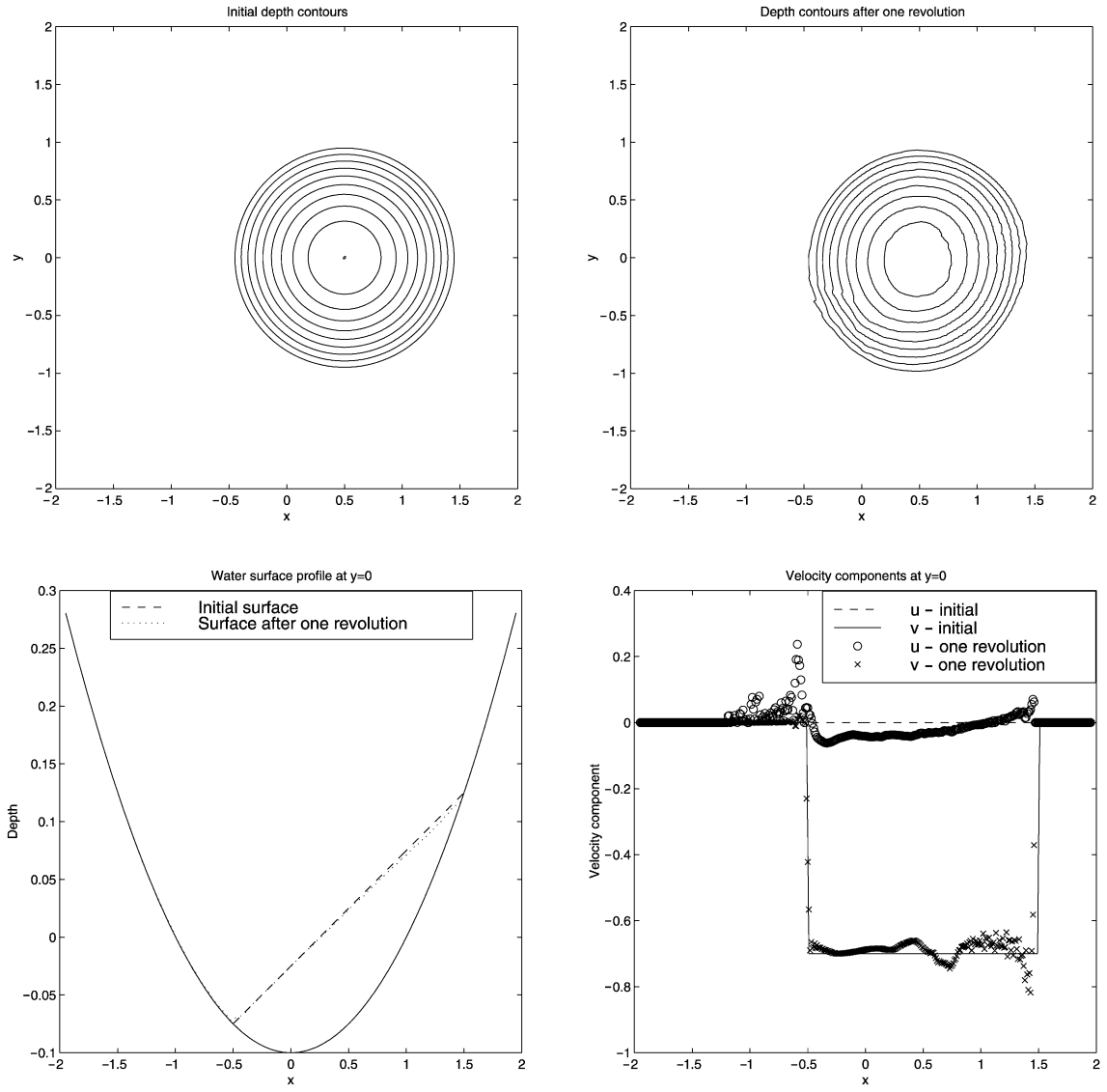

Fig. 7. Comparison of the numerical approximation to the flow around a parabolic basin with the exact NLSW solution after a single revolution (the same as the initial conditions). The top two diagrams show contours of water depth for both exact and approximate solutions. The bottom two give comparisons of free surface elevation, overlaid on the bed geometry, (left) and velocity components (right) along the line $y=0$.

Kirby (1997). Here we take $L=10$ m, define $\eta_0=0.0255$ m on a depth $h_0=1.273$ m (where η_0 is the initial solitary wave height), so that $\eta_0=0.02\ h_0$ and the solitary wave is nonbreaking (see Özkan-Haller and Kirby, 1997). This means that the position of the flat section is at $x=9.55$ m. In the numerical experiment, $d_{\mathrm{tol}}=0.00005$ m, and for the purposes of output, $d_{\mathrm{shore}}=0.0002$ m, so that the values are small enough compared to the offshore depth to effectively provide a $d=0$ condition at the shoreline ($f_{\mathrm{w}}=0.0$). Increased resolution is achieved by using $\xi_{\mathrm{crit}}=0.05$. The *min-mod* flux limiter is used here. The maximum level of refinement is 4. The coarse grid is defined over an area $0\ \mathrm{m}<x<30$ m, $-10\ \mathrm{m}<y<10$ m and has 20 cells in each direction. The solitary wave is defined at the offshore boundary as a time series of surface

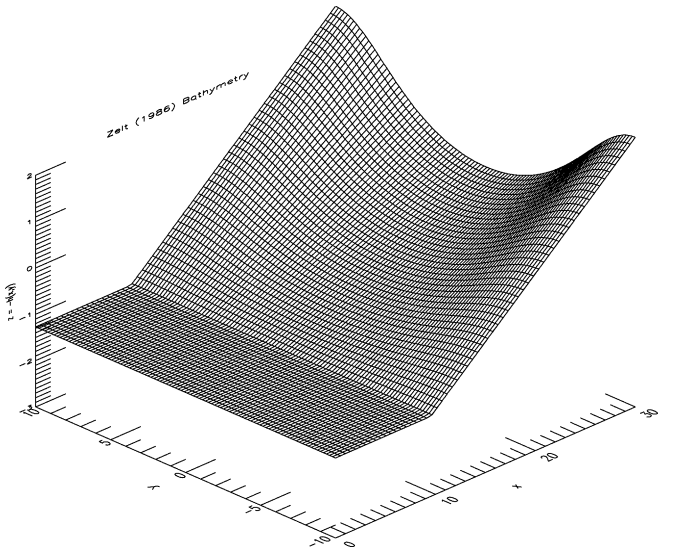

Fig. 8. Bathymetry of the 2D run-up test of Zelt (1986).

elevations with velocity given by shallow water theory at $x=0$, at which location there is an absorbing/generating boundary. The lateral boundaries are reflecting.

Two comparisons with the solution of Özkan-Haller and Kirby (1997) are made: the time-varying run-up at five different alongshore (y) locations (Fig. 9), and the maximum run-up and run-down over the simulation (Fig. 10). In these figures, the shoreline is defined as being at the center of the last wet cell. If we identify such a cell with indices (i,j), then the vertical run-up value at that cell is defined as $\eta_{i,j}$ ($=d_{i,j}-h_{i,j}$). Implicitly, therefore, the actual moving shoreline is interpolated horizontally onto the beach, although no actual interpolation is attempted in the present code or analysis. The predictions of the moving shoreline shown in Fig. 9 are close to those of Özkan-Haller and Kirby (1997) overall. Differences are primarily in a small phase lag and some more, small oscillations in the present solutions. The oscillations are due in part to the inherently discrete nature of the shoreline modeling, in which cells are filled or drained depending on the local fluxes (and the fact that the grid resolution is continually changing throughout the domain), and also probably because the present code uses no numerical filtering (Özkan-Haller and Kirby, 1997, use a 16th-order filter of the type described by Shapiro, 1970). Other probable sources of differences are due to the different source term discretization in the present model and because the flux conservative form of the equations are being solved. Note also that in the present simulation the actual y/L values were slightly different. This is because of the adaptive nature of the code, in which cells are repeatedly subdivided. Since variable quantities are stored at cell centers this means that interpolation must be used to reconstruct values at required locations. Instead, here, values at centers of all shoreline cells are output and those cell centers closest to the required locations are output. The actual positions are shifted $y/L=0.003$ (for the $y/L=0,\ldots,0.75$) and $y/L=-0.003$ (for $y/L=1.0$). This translates to a dimensional distance of 0.03 m, but this difference is not considered large enough to account for the differences noted. A more likely reason for the phase lag discrepancy is the position of definition of the solitary wave. In the simulation of Özkan-Haller and Kirby, the finite computational domain corresponds to a semi-infinite physical one, so the offshore boundary nominally corresponds to $x=-\infty$. As previously mentioned, the offshore boundary in the present model is at $x=0$, 9.55 m seaward of the slope.

Despite these differences, the overall correspondence between the present model and the runs of Özkan-Haller and Kirby (1997) is good. Although it is difficult to tell, it appears that the differences, apart

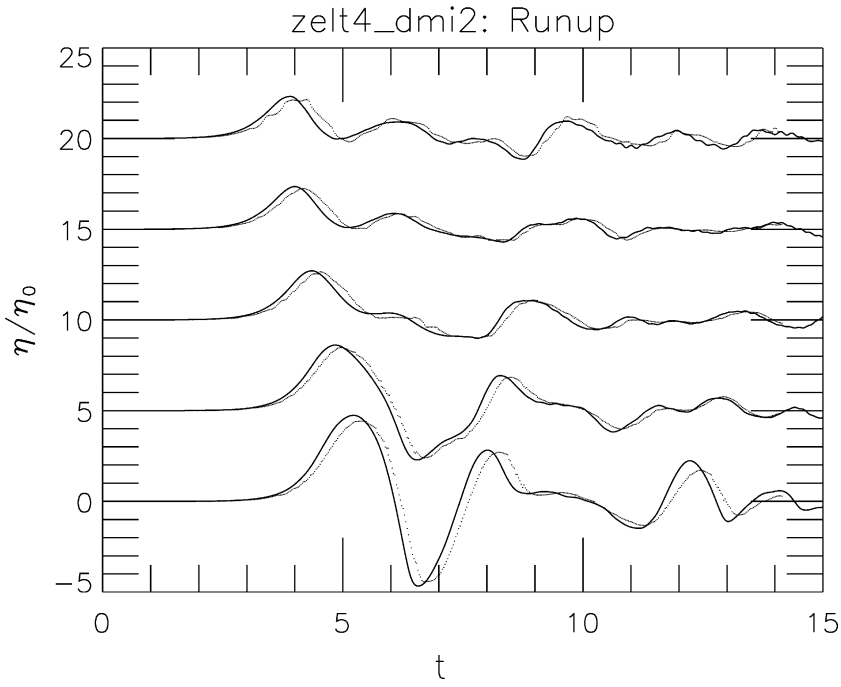

Fig. 9. Time series of run-up at five alongshore (y) locations. Solid line indicates the solution of Özkan-Haller and Kirby (1997); the dotted line is the present method.

from the phase lag, are similar in size to those between Özkan-Haller and Kirby (1997) and Zelt (1986) (see Özkan-Haller and Kirby, 1997).

The predictions of the maximum run-up and run-down (Fig. 10) are close to those of Özkan-Haller and Kirby (1997). The envelope, which represents the predictions of the model of Özkan-Haller and Kirby (1997), is very close to an envelope that would be constructed around the run-up predictions of the present model. There are only two significant discrepancies: the first is a slight underprediction of the maximum run-up, which is accentuated in the middle of the bay, and there is also a similar underprediction of run-down. These discrepancies are consistent with the method chosen here to indicate a shoreline location (and therefore run-up value): horizontal interpolation from the center of the last wet cell. In fact, the true run-up position would be found at a slightly higher value, as shown by the envelope of Özkan-Haller and Kirby (1997). Overall, the present results appear to be very close to those of Zelt (1986), although the results of Özkan-Haller and Kirby (1997) appear to give a higher run-up than those of Zelt (1986). These were not available for the present tests, but can be inspected in Özkan-Haller and Kirby (1997).

It must also be remembered that the present code is designed with robust shock modeling in mind, and includes the facility for multiple shorelines. As such the comparisons shown in Figs. 9 and 10 were considered satisfactory.

4.5. 2D datasets

Briggs et al. (1995) performed a series of experiments of tsunami run-up at the US Army Engineer Waterways Experiment Station in a 30 × 25-m basin, with a conical island situated at its center. A directional wave generator produced plane solitary waves of specified crest lengths and heights propagating toward the island. Twenty-seven wave gages were distributed around the island and the highest excursion of the shoreline was measured at 20 locations around the island after each solitary wave run. A subset of these tests was used as a benchmark test for the International Workshop on Long Wave Run-up (Yeh et al., 1996), which constituted Benchmark Problem 2 of Yeh et al.

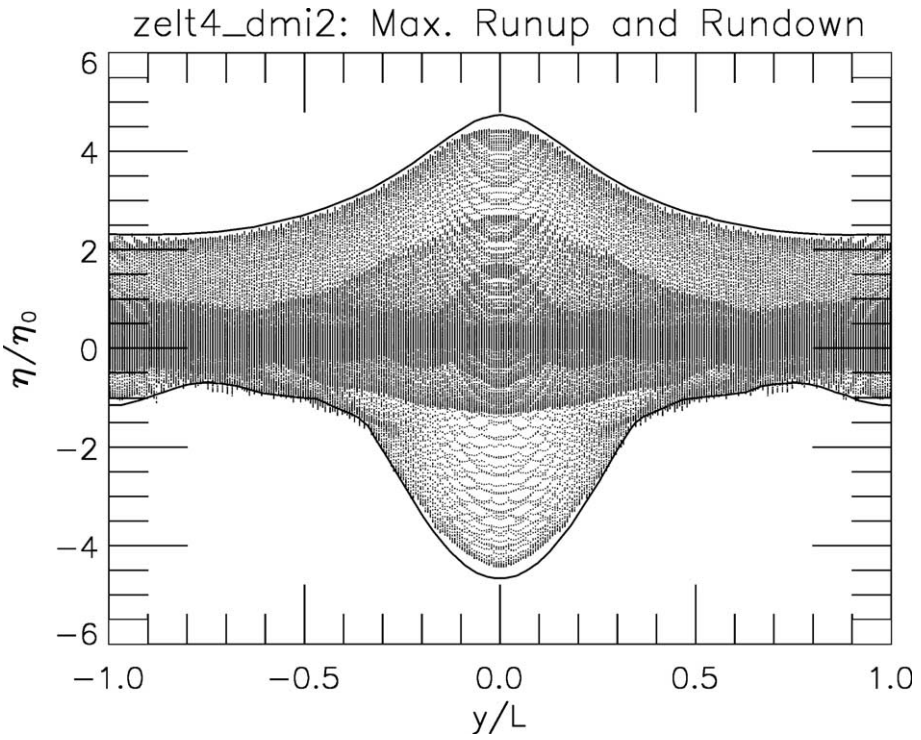

Fig. 10. Run-up in 2D: maximum and minimum run-up. Dots indicate the surface elevation ($d(x,y,t) - h(x,y)$) at the center of each shoreline node. The solid line is the maximum run-up and run-down found by Özkan-Haller and Kirby (1997).

(1996) (see Briggs et al., 1996), against which a number of numerical models (Masamura and Fuijima, 1996; Takagi, 1996; Titov and Synolakis, 1996) were tested. Here we compare the present model with the measured data, both free surface elevation at the four wave gages specified in the Benchmark Tests, and maximum run-up around the island. The predictions of the other models were not available for direct graphical or numerical comparison, but the simulations of OTT-2D are discussed with relation to the other numerical results.

A sketch of the bathymetry is shown in Fig. 11. Fig. 12 shows a plan view of the basin, including the positions of the four wave gages (numbers 6, 9, 16 and 22 of the original tests) that were used to compare models in the intercomparison exercise (although Titov and Synolakis, 1998, subsequently presented comparisons with far more gages). Also shown is wave gage 3, measurements from which were originally provided to participants in the testing for input purposes (see Briggs et al., 1996). We compare with measurements at these five gages. A total of three solitary waves were generated. We compare with two of these: cases B and C, which had solitary waves of target heights 0.1 and 0.2 m, and are suitable for comparison because B was nonbreaking (apart from gentle spilling near the shoreline) whereas C broke prior to encountering the shore.

Numerical solution was effected on a domain $0 < x < 25$, $0 < y < 30$ m, which is the same size as that of Titov and Synolakis (1996). A coarse grid of 20×20 cells ($\Delta x = 1.25$ m, $\Delta y = 1.5$ m) was used. Five levels of refinement were allowed with factors of refinement set to 2 in each direction, so that the finest cell size possible was $\Delta x = 0.0391$ m, $\Delta y = 0.0469$ m, similar in magnitude to the finer nested grid used by Titov and Synolakis (1996). The other numerical models also used irregular or nested grids. Titov and Synolakis (1996) used a coarser grid of $\Delta x = \Delta y = 0.28$ m and a finer, nested grid over the sloping beach of the island of $\Delta x = \Delta y = 0.09$ m. Takagi (1996) used a triangular, finite element grid that gradually increased

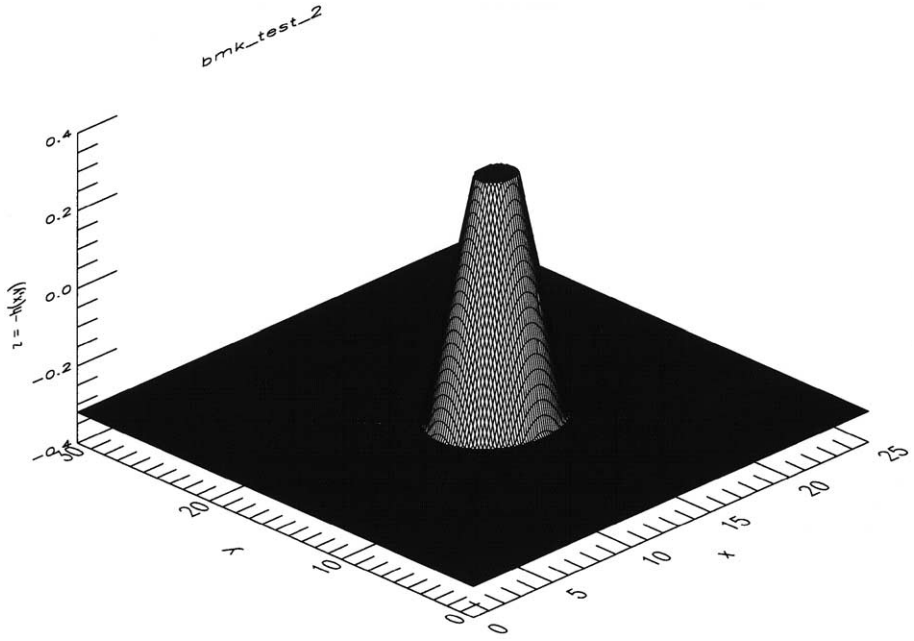

Fig. 11. Wave basin bathymetry in the experiment of Briggs et al. (1995).

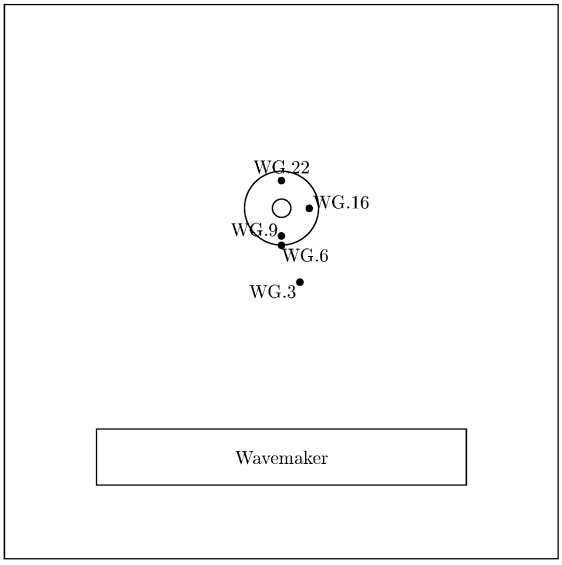

Fig. 12. Wave basin experiment of Briggs et al. (1995). The coordinate system has an origin located at the right end of the wavemaker. The conical island is then centered at (12.96, 13.80 m). See Briggs et al. (1996) for the locations of the gages relative to this coordinate system.

element density toward the center of the grid (island), from an element size of about 0.6 m (by inspection of Fig. 1 of Takagi, 1996) to about 0.05 m at the shoreline. Masamura and Fuijima (1996) used a 3D model, with $\Delta x = \Delta y \approx 0.30-0.40$ m towards the outer boundary and $\Delta x = \Delta y = 0.10$ m near the island. We use a minimum depth $d_{\text{tol}} = 0.0001$ m with a shoreline depth $d_{\text{shore}} = 0.001$ m and set $f_w = 0.0$ and $\xi_{\text{crit}} = 0.05$ in these computations, which were carried out with the *minmod* flux limiter. At the boundary $x = 0$, we define an absorbing/generating boundary, and input the velocities ($U_0(t)$) derived directly by differentiation of the paddle positions for tests B and C (Briggs et al., 1996). The signals thus obtained showed some noise, because of round-off error, apparently, but we made no attempt to smooth these signals. This was considered the best approach given the inevitable discrepancies between the actual bathymetry and the synthetic one. $\eta_0(t)$, the free surface elevation at the boundary, was specified through the relation $\eta_0(t) = \sqrt{h_0/g}U_0(t)$.

In Fig. 13, we show the model predictions for case B compared with the measurements. Note that only 20 s of the test is run. This is because after this time wave motions are dominated by smaller period (dispersive) wave motions (see Briggs et al., 1995; Yeh et al., 1996),

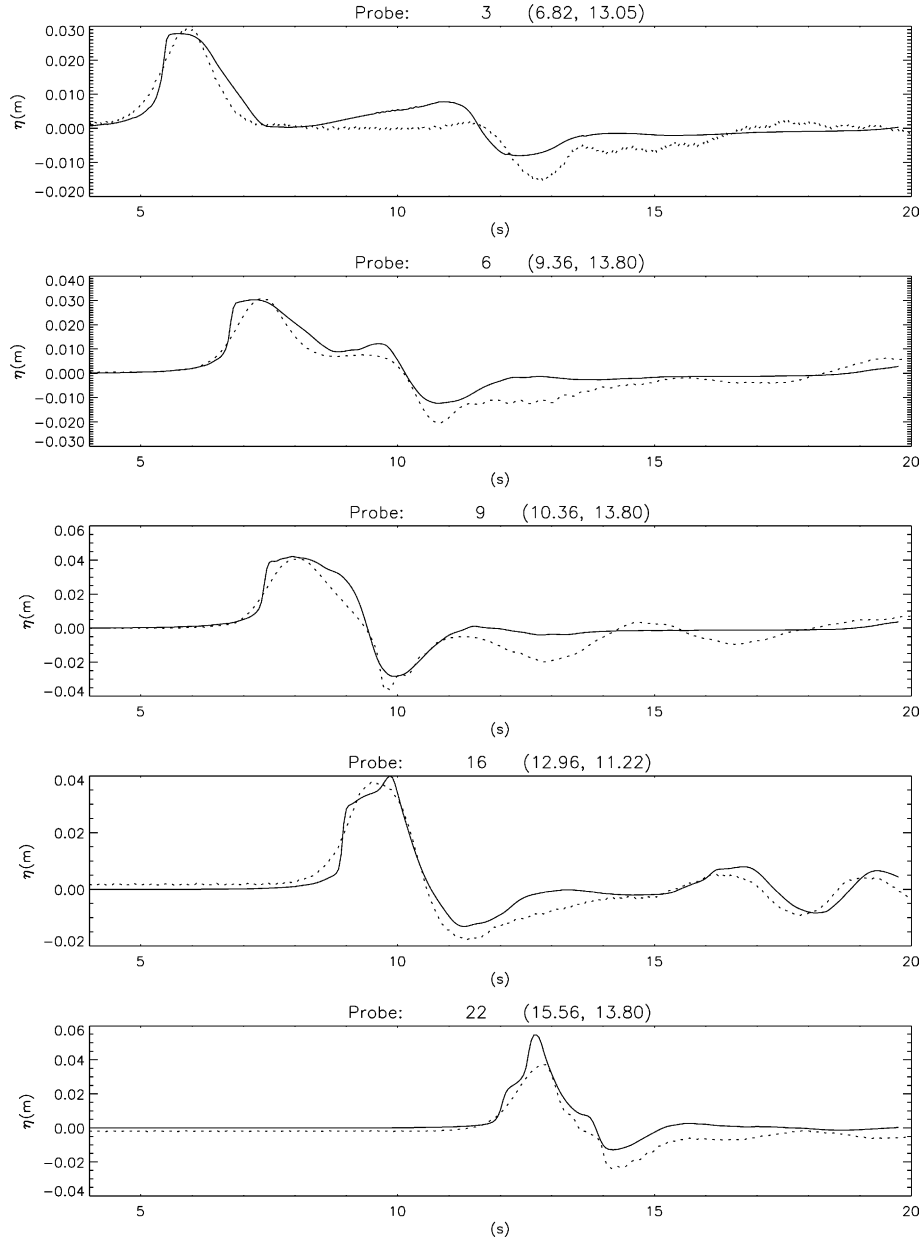

Fig. 13. Predicted (solid line) and measured (broken line) free surface elevation at wave gages 6, 9, 16 and 22 of Benchmark Problem 2B of Yeh et al. (1996).

which the NLSW equations cannot model. Therefore, we focus only on the initial run-up inundation and run-down process. It can be seen that the model does a reasonable job of modeling the water depths. The major differences are that it steepens the wave front earlier than in reality. This effect can be seen first at WG.3, at which location the measured time series indicates that the solitary wave is still largely symmetric, whereas the numerical wave appears to have steepened. At WG.6, WG.9 and WG.16, this effect can also be seen,

although the wave heights and the overall form of the signals are reproduced reasonably well. At WG.22, the wave height is overpredicted. Another discrepancy is in the wave trough behind the initial front, which is underpredicted at all gages. These discrepancies are consistent with the NLSW equations themselves, and the steeper wave front at, for instance, WG.3 is due to the absence of dispersion in the NLSW equations. In the NLSW system, waves always break if propagated over a sufficiently large distance; in reality however, dispersive effects are present, which act to stabilise the wave. If the simulations were to be run from the position of WG.3 then the effect of steepening would be less pronounced at the later gages. The present results seem similar (as far as can be judged) to those obtained by Takagi (1996), whereas those obtained by Titov and Synolakis (1996) (see also Titov and Synolakis, 1998, for a more comprehensive comparison) are closer to those recorded. This difference in codes based on the same equations is noteworthy and will be discussed later. Masamura and Fuijima (1996) also obtain slightly better modeling of the wave shape than the present model, although there are still notable discrepancies between their results and the measurements, particularly in the trough region. However, the 3D nature of their model makes it unlikely to be competitive in terms of the computing power required to estimate quantities of interest to coastal engineers to an appropriate accuracy, even though it would allow a more detailed analysis of the fluid dynamics. So we neglect this model from now on.

The maximum run-up is compared with the measured values in Fig. 14. There is a slight overprediction around the front of the island, which might be due to

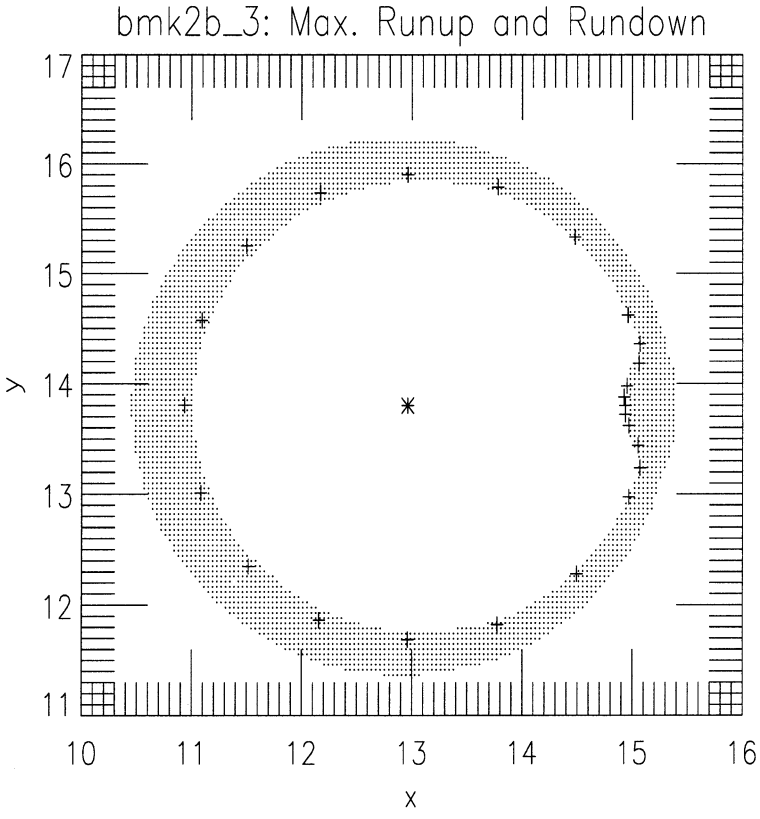

Fig. 14. Predicted (dots) shoreline positions for case B of Benchmark Problem 2 of Yeh et al. (1996). Thus, the dotted region shows the region between maximum run-up and run-down during the run. The crosses denote the measured positions of maximum run-up. Note that each dot corresponds to the center of a wet cell at the shoreline.

the absence of bottom friction in the present runs, but that in the lee of the island is close to the recorded value.

In Fig. 15, we show the equivalent model predictions for case C compared with the measurements. This is similarly different in detail but, by WG.16 and WG.22, actually better than that in the earlier test. In Fig. 16, the corresponding run-up predictions are shown, and they are also in better agreement with those recorded than in the previous case.

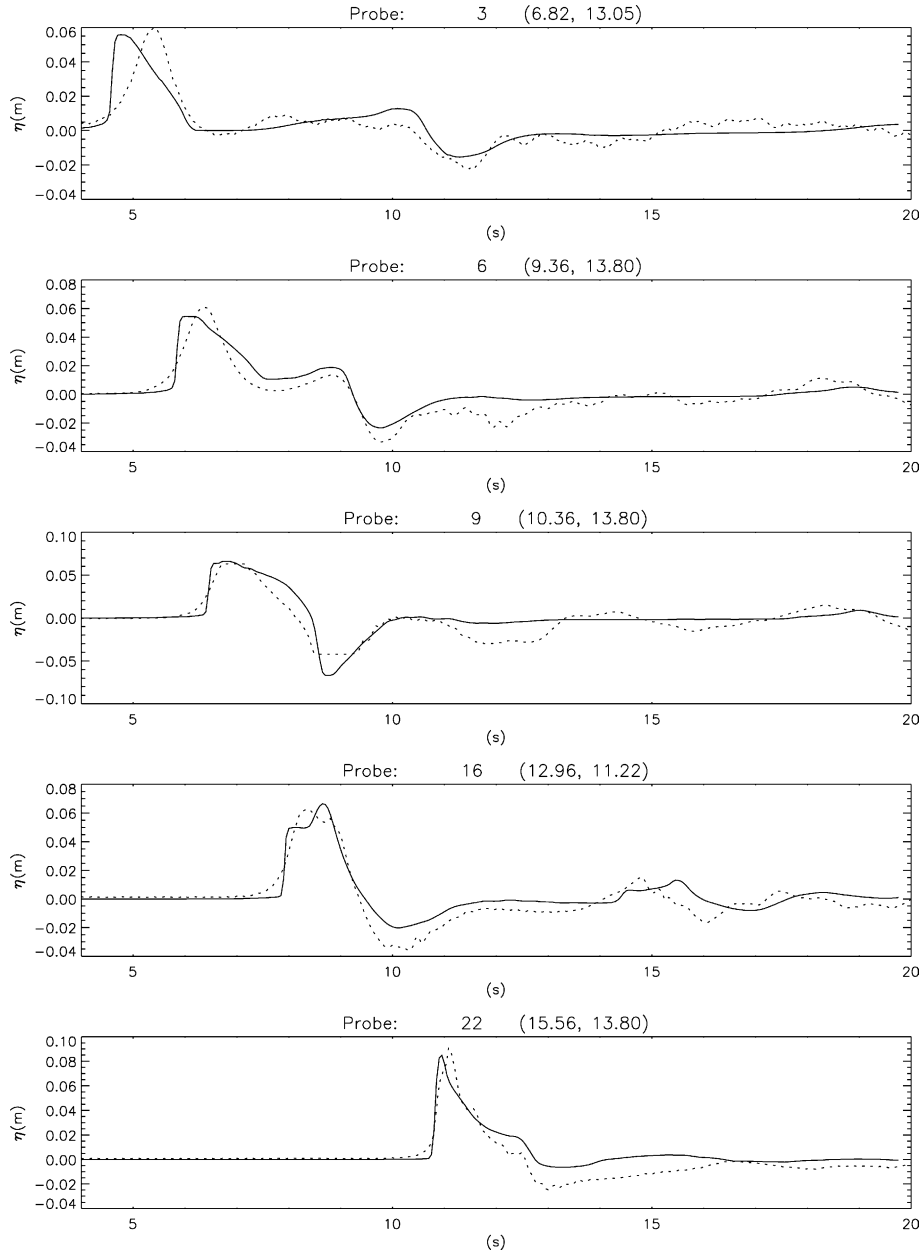

Fig. 15. Predicted (solid line) and measured (broken line) free surface elevation at wave gages 6, 9, 16 and 22 of Benchmark Problem 2C of Yeh et al. (1996).

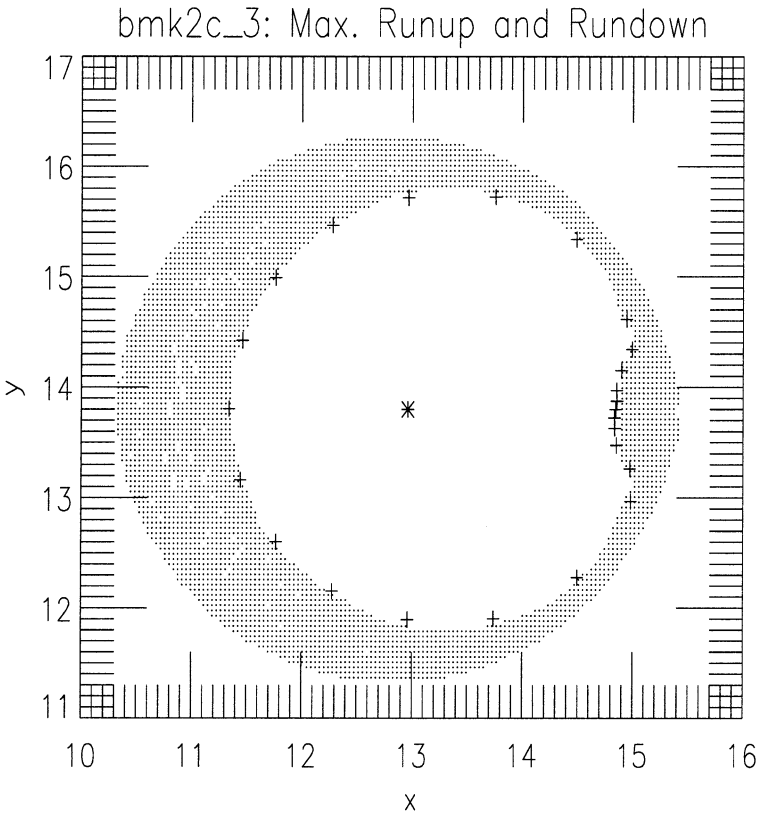

Fig. 16. Predicted (dots) shoreline positions for case C of Benchmark Problem 2 of Yeh et al. (1996). Thus, the dotted region shows the region between maximum run-up and run-down during the run. The crosses denote the measured positions of maximum run-up. Note that each dot corresponds to the center of a wet cell at the shoreline.

The adaptive grids created by OTT-2D are illustrated in Fig. 17, which show the meshes comprising the grids at each level as the solitary wave propagates in from the generating boundary. Note that the finest level of refinement (level 5) is achieved on both flanks of the wave, although the grid system is significantly asymmetric at this time. In Fig. 18, the grid system after the wave has passed over the island is shown. The finest level of grid indicates the position of the waves refracted around the sides of the island, which have also passed through each other at this point.

The reason for the improvement in correspondence between predictions and measurements may be found in the larger initial wave height of the wave in case C. Although at WG.3 the measured wave still seems symmetric, whereas the numerical wave appears to have broken, the physical wave does in fact break

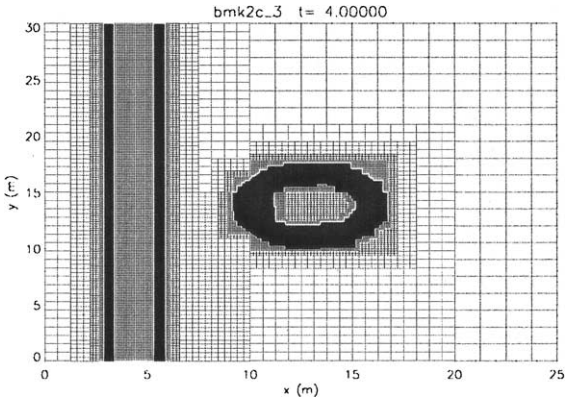

Fig. 17. The grid and mesh system at one time ($t=4$ s) during the simulation of Case C of Benchmark Problem 2 of Yeh et al. (1996). The coarse grid (20×20 cells) can be seen on the right.

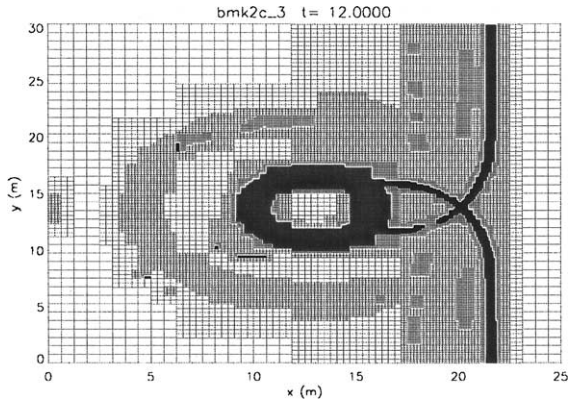

Fig. 18. The grid and mesh system at one time ($t = 12$ s) during the simulation of Case C of Benchmark Problem 2 of Yeh et al. (1996). The coarse grid (20×20 cells) is completely covered by finer grids here.

before encountering the shoreline. In such a regime, the NLSW equations provide a good modeling capability, and the shock modeling of the present code appears accurate. It results in good accuracy in wave heights in case C, albeit with some phase error, due in part to the aforementioned discrepancies. In case C, the model of Titov and Synolakis (1996) (VTCS-3) shows more discrepancy with the signals recorded. That code is first order in time and not based on the conservative form of the equations (see Titov and Synolakis, 1995, for a more detailed description of their method), which naturally impose the correct shock conditions, and Titov and Synolakis (1995) note errors in mass conservation when waves break. The code of Takagi (1996) seems somewhere between the present results and those of Titov and Synolakis (1996). The close agreement between model and measurements on maximum run-up is evidence of good shock modeling. The results of Titov and Synolakis (1996) show more discrepancies here than in case B, where they obtain close agreement with measurements (see Fig. 3 of Titov and Synolakis, 1996 or Fig. 4 of Titov and Synolakis, 1998).

This difference between the results provided by two different models of the same equations should be noted, since Titov and Synolakis (1996) also introduce their solitary waves at the same location and use the prerecorded paddle positions and, in theory, there should be a unique solution to a properly posed mathematical problem. On the other hand, it must be borne in mind that the schemes are substantially different, and even if convergence between the two schemes were to be assured in the limit $\Delta x \to 0$, we are restricted to working with finite grids, so significant differences are to be expected. For nonbreaking waves, the characteristic form approach of Titov and Synolakis (1995) seems to work very well. In the present model, wave breaking occurs earlier. One possible explanation is that, although similar, the generating boundaries are not the same (although it should be remembered that the present model does reproduce the nonbreaking Carrier–Greenspan solution well). However, this effect is small, since in the vicinity of the model boundary of OTT-2D (not shown) the waves do have the correct shape. More likely is that the VTCS-3 code is 1st-order accurate in time—the present code is 2nd-order accurate—and possibly numerically more dissipative. Another possible explanation is the difference in the source term discretization. It should also be noted that the Lax-Wendroff method, on which the present solution scheme is partially based, tends to introduce a slight phase lag (see e.g. Hirsch, 1990). This does not seem to be an issue in this comparison, but it may also explain the small discrepancy in the comparison with Özkan-Haller and Kirby (1997) (see Fig. 9).

Overall, results show reasonable agreement with measurements, particularly in case C. The discrepancies with measurement are explainable by the absence of frequency dispersion in the NLSW equations, and therefore in the code.

At this point, it is worth emphasising the value of the adaptive mesh refinement. The above results were obtained on a 20×20 coarse grid with five levels of refinement, each by a factor of 2 in both directions. The same calculations could also be carried out on a uniform 640×640 grid, which has an equivalent resolution to the finest grid level in the adaptive computations. For problem 2B, the fine grid calculation took 9.1 times as long to carry out and used more than three times the memory, largely because the adaptive calculation never required more than 20% of the number of cells of the fine grid. The improvement for problem 2C is slightly less impressive because the wave is larger and a larger proportion of the grid is required to be fine, but the amount of cpu time taken was still reduced by a factor of almost 5.

5. Overtopping by obliquely incident waves

This section is included as a novel application of the numerical model presented and validated in the previous sections of the paper, which has not been studied in detail elsewhere in the literature.

5.1. Physical tests

Between December of 1978 and the same month of 1979, a series of overtopping tests (referred to here as the Q1425 tests) were performed in a wave basin at HR Wallingford, which were commissioned by the then Severn-Trent and Wessex Water Authorities and the Central Electricity Generating Board as part of a major study to determine flood defence levels in the lower Severn basin. As part of this study, tests were conducted in a wave basin at scale of 1:25 in order specifically to examine the effect of offshore wave angle of incidence on overtopping rates at smooth, sloping sea walls, with and without berms. The basin layout, at prototype scale, was of a flat floor at -8 m still water level (SWL), which then rose at a constant 1:20 slope to -4 m SWL at the toe of a sloping sea wall. The sea walls were constructed of smooth plywood, and the slopes examined here are 1:1 and 1:4. A 15-m-wide (model scale) single wave paddle then generated long-crested random wave time series (JONSWAP); wave guides (effectively solid, vertical walls) were added to create an additional 2-m-wide calibration channel with the same foreshore slope but no structure in place, and with a shallow permeable spending beach at the end. The wave paddle was positioned at an angle (mostly either 0°, 15°, 30°) to the sea wall crest, and a series of sea wall sections was tested. Here we consider two sections (1:1 and 1:4 slopes), each without a berm. In the physical tests, overtopping water was collected via a 1-m-wide chute immediately behind a central portion of the sharp sea wall crest (there was no flat portion on the crest). Numbers of waves overtopping were measured using three overtopping counters. The sea wall crest was 150 m long (prototype).

The test procedure was to run the paddle for a particular test for $300T_z$ (mean crossing periods) before taking five samples $100T_z$ long, each separated by intervals of $200T_z$. Overtopping rates and numbers of waves were based on averages over these separate collection times.

These tests were used to compile a design manual (Owen, 1980), including parametric overtopping formulas, which were subsequently disseminated more widely by Owen (1982). These formulas reflected one interesting aspect of the test results: maximum overtopping rates were frequently achieved not at normal incidence but at "small" oblique angles, say 15° or 30°.

To the authors' knowledge, no subsequent tests have shown a similar relationship, and there does not appear to be an obvious explanation for this behavior. Here we use OTT-2D to see if we can reproduce these results and observe a similar relationship.

5.2. Numerical model tests

The main difference between the physical and the numerical tests is that in the latter waves could not be run from a location equivalent to the paddle position. This was because at that position the still water depth and peak (or mean) frequency defined wave conditions of intermediate depth, and the paddle was located far enough away from the toe of the sea wall slope for frequency dispersion effects to have a significant effect on the waves before they reached the structure. Since the NLSW equations do not accommodate these kinds of motions, a different approach was taken, with the offshore (numerical paddle) conditions (specified in terms of H_s, significant wave height, T_m, mean wave period, and θ, the offshore angle of incidence) being transformed to equivalent conditions at a smaller distance, 10 m, seaward of the sea wall toe, using linear theory (T_m was first converted to T_s, significant wave period, using the approximate relation $T_s = 1.2T_m$). The original conditions and the transformed ones are shown in Table 2. Also shown there are the actual H_s and T_m values recorded in the synthetic OTT-2D time series. It should be noted that we only ran one simulation for each of the tests (as opposed to five), so more variations are to be expected in the OTT-2D results than in the tests.

Each test was run for $100T_s$. The tests were run with a fixed (unrefined) grid of 135 by 100 computational cells in the x and y directions, respectively, covering a distance of 50 [-10.0,40.0] and 400 [0.0,400.0] m in the x and y directions, with $d_{tol} = 0.0001$ m, and

Table 2
Test results for the four series taken from the Q1425 wave basin overtopping tests conducted at HR Wallingford in 1978 and 1979

Test name	Slope	θ (°)		H_s (m)		T_m (s)		$\overline{Q}$ (l s^{-1} m^{-1})	
		Target	Transformed	Test	OTT-2D	Test	OTT-2D	Test	OTT-2D
A101R	1:1	0	0	1.39	1.41	3.96	4.18	6.5	16.3
A104	1:1	15	12.5	1.40	1.37	3.99	4.03	9.1	17.1
A107	1:1	30	24.3	1.32	1.32	3.97	4.07	5.2	1.6
A102R	1:1	0	0	1.90	1.83	4.61	4.70	32.5	48.3
A105	1:1	15	12.1	1.96	1.91	4.64	4.97	43.3	45.0
A108	1:1	30	23.4	1.89	1.87	4.66	4.92	25.7	22.6
A402RR	1:4	0	0	1.77	1.72	4.55	4.76	4.2	6.5
A405	1:4	15	12.2	1.73	1.68	4.57	4.51	5.1	1.6
A408	1:4	30	23.5	1.77	1.86	4.63	4.95	5.1	0.2
A403R	1:4	0	0	2.55	2.46	5.29	5.47	20.1	76.8
A406	1:4	15	11.9	2.30	2.35	5.22	5.66	26.3	38.6
A409	1:4	30	23.0	2.40	2.39	5.22	5.57	30.3	17.6

Note that both the target and transformed values of θ are given. H_s and T_m values from the OTT-2D runs were obtained by zero-upcrossing analysis. The figures here relate to prototype scale and a 1:25 scaling has been used.

$f_w = 0.02$, based on the tests of Dodd (1998). An unrefined grid was used to ensure that there were no differences between the 1:1 and 1:4 tests based on differences in the refinement flag relative to the different slopes. No further tuning to the problem in hand was undertaken.

Waves were generated at the seaward (west) boundary with the east boundary being absorbing. The south boundary ($y = 0.0$ m) is reflective and the north ($y = 400.0$ m) absorbing. It was not possible to impose truly periodic boundaries since that would require nonrandom waves, so the present configuration is equivalent to a wave guide/vertical wall on the southern boundary and an open boundary to the north. The layout (for the 1:4 sea wall slope) is shown in Fig. 19. Note that the numerical wave paddle is always perpendicular to the sea wall, so that in the model the wave angle, θ, is varied. The other approach to this situation would be to vary the orientation of the bathymetry. This is best avoided because it would result in waves from one end of the numerical paddle travelling further than those from the other end before encountering the structure, and therefore evolving further toward breaking.

Only a subset of all the Q1425 tests was run. It was decided that these tests should be those without a berm, as those were the only sets including an extensive variation in wave angle. These sets were of overtopping tests of a 1:1 and 1:4 slope. Each had a small flat crest, on which the numerical overtopping probes were located. Both bathymetries were subject to a shadow region at the up-wave (south) lateral boundary, because the wave guide (solid wall) is not aligned with the incoming wave (apart from normal incidence). This shadow region was accounted for in the overtopping analysis by ignoring the region close to the

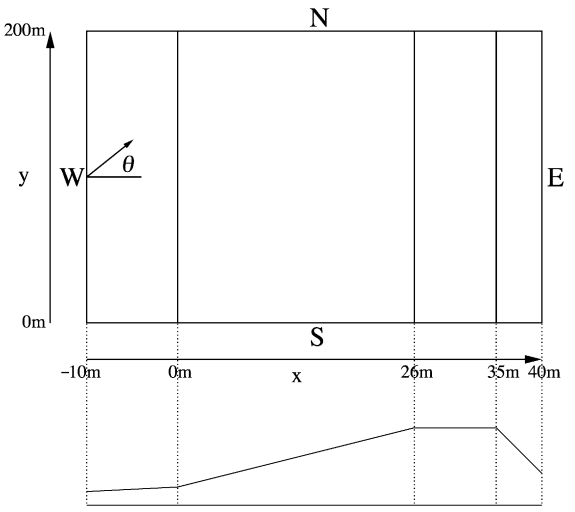

Fig. 19. Plan view and cross-section of the numerical wave basin for the (1:4) Q1425 2D overtopping tests.

south boundary in the overtopping analysis. This analysis was based on a series of numerical probes strung along the crest of the sea wall, so as to observe any along-wall dependence of overtopping rates/volumes. These probes were situated just leeward of the shoreward edge of the sea wall crest ($x = 26.9$ m). Probes were also located on the offshore (west) boundary and at the toe of the sea wall. In fact (and reassuringly), the alongshore variation of overtopping rates was negligible outside the shadow region (tests were also performed with a 200-m-wide basin, which showed no significant difference). Here we present results from the central gage (at $y = 200$ m). Overtopping rates in the numerical simulations were measured based on the x-component of the flux (dU), and a minimum depth of 5 cm was assumed in the overtopping event counting analysis.

The tests considered are summarised in Table 2, with their measured and numerically simulated mean overtopping rates. It can be seen that whereas in the measurements a peak in Q at off-normal incidence is generally apparent, it cannot in general be seen in the numerical tests. There is a small off-normal peak in the model simulations for the A101R series, although a series of random tests would have to be run before it can be established that the result is significant. The results from the A102R series show results between 0° and 15° being very close. It therefore seems that model runs for the 1:1 slope structure do at least indicate comparable overtopping rates between the two first angles. Indeed, the wave basin test runs and the model run results are very close for the A105 and A108 runs. Overall, model mean overtopping rates are reasonably close for the 1:1 slope structures.

Model runs for the 1:4 slope show a dissimilar trend from that found in the wave basin tests, with mean overtopping rates falling away sharply for more oblique angles, whereas the wave basin tests showed peak or joint peak values at 30° incidence. There is a tendency to overpredict at normal incidence (the A403R test shows a large overprediction) and to underpredict at 30° incidence. Nevertheless, predicted rates are of a reasonable order of magnitude.

Finally, these physical model tests, at least those undertaken on the 1:1 slope, also comprise a demanding test for a model based on the NLSW equations. These equations implicitly assume a mild bottom slope, which a 1:1 gradient clearly does not provide. However, Hu et al. (2000) have already shown that these same equations can give reasonably accurate simulations on slopes far in excess of the present gradients, so it is not too surprising that, even without a calibration, reasonable results are found.

There are a number of possible reasons why we are not seeing an off-normal peak in the mean OTT-2D overtopping rates. One reason is suggested by the comparatively poor performance of the model for the 1:4 slope. The 1:4 slope structure compels each wave to travel further and, in the NLSW system, therefore means that each wave will have longer to become a bore (shock) and thereby decay in height. In reality, this will not necessarily be so, because the wave may not break as early on the (effectively) shallower approach slope experienced by the obliquely incident wave. Indeed, this (shallower effective slope) seems like a possible explanation of the larger overtopping rates recorded in the original tests. It should also be noted that although the H_s values from the synthetic time series are generally close to the target values, the T_m values are mostly overestimated. This is probably because of the crudeness of the relation $T_s = 1.2T_m$ that was used, and this increase in period probably accounts for at least part of the overestimation of the overtopping rates at normal incidence, another reason perhaps being the value of f_w assumed, which, it should be recalled, was taken from other tests.

The other main reason is numerical. In the cases where the waves are obliquely incident to the shore the dominant flow direction and solution gradients are not aligned with the grid, leading to a larger amount of numerically induced diffusion and, potentially, a damping effect on the waves. This would cause obliquely incident waves to give less overtopping relative to the experiment than the normal incidence waves.

Finally, it is worth noting that the wave basin tests being examined are the only tests known to the authors that show such off-normal peaks in mean overtopping rates. It would therefore seem to be desirable to perform similar physical tests to examine this issue before investigating the observed discrepancy further.

6. Discussion and conclusions

A 2D numerical model suitable for coastal engineering applications has been presented. Being based

on the (2D) NLSW equations, it is suitable for problems that do not require the modeling of frequency dispersion, such as wind wave run-up, overtopping and flooding, as well as tsunami inundation. The model is adaptive (using a standard Cartesian AMR algorithm), and the finite volume technique on which it is based enables simple modeling of complicated geometrical situations, which are often encountered in real coastal engineering problems. The model performs satisfactorily in all the validation tests on which it is run.

These tests comprise a substantial verification for OTT-2D. While in certain individual tests other numerical approaches seem to give better modeling, the present model performs well overall, and deals with both idealized bathymetries and realistic situations with nonuniform, complex bathymetries, in which circumstances many of the other models mentioned here would not cope (and for which circumstances they were not designed). The present model is robust: it never crashed in a nonadaptive computation, and the bathymetries examined here are all amenable to adaptive grid implementation. Moreover, this adaptivity provides substantial savings in CPU time and memory. A speed-up by a factor of between 5 and 10 is routinely attained, compared with using a uniform mesh of equivalent fine resolution, with little deterioration in accuracy. The savings in required memory are slightly less, but still of significant value.

The overtopping tests, which it has been used to simulate, show a distinct peak in overtopping rate at oblique angles of incidence (usually 15° for 1:1 slopes and 15/30° for 1:4 slopes). However, the model fails to reproduce this peak in all but one of the tests. It is not clear whether this is due to modeling deficiencies (numerical waves decaying too much because of the increased distance over which they propagate and additional numerical dissipation which occurs when the flow is oblique to the grid) or perhaps that they are simply agreeing with other, subsequent studies, which suggest that such a peak does not exist. Overall, however, predicted mean overtopping rates are similar to those observed. These fairly steep (1:1) slopes also provide another example of the NLSW equations giving reasonable engineering predictions beyond their apparent regime of validity.

Acknowledgements

The UK Ministry of Agriculture, Fisheries and Food provided the financial support for this work. The authors would also like to thank Andy Steele of HR Wallingford, for retrieving the 1978–1979 overtopping test data, as well as discussing the tests extensively with ND. They are also grateful to Mike Briggs of the US Army Waterways Experiment Station at Vicksburg, MS, for making available the data from the circular island tsunami wave basin test; and to Tuba Özkan-Haller, of Oregon State University, who provided the results of her computations for the Zelt case. Much of the work presented here was done when the authors were at Reading University and HR Wallingford, respectively. The authors would like to thank both institutions for their support.

References

Alcrudo, F., Garcia-Navarro, P., 1993. A high-resolution Godunov-type scheme in finite volumes for the 2d shallow water equations. Int. J. Numer. Methods Fluids 16, 489–505.

Berger, M.J., Colella, P., 1989. Local adaptive mesh refinement for hyperbolic partial differential equations. J. Comput. Phys. 82, 67–84.

Berger, M.J., Oliger, J., 1984. Adaptive mesh refinement for hyperbolic partial differential equations. J. Comput. Phys. 53, 484–512.

Besley, P., 1999. Overtopping of seawalls: design and assessment manual, R&D Report W 178. Environment Agency, North East Region.

Briggs, M.J., Synolakis, C.E., Harkins, G.S., Green, D.R., 1995. Laboratory experiments of tsunami run-up on circular island. Pure Appl. Geophys. 144 (3/4), 569–593.

Briggs, M.J., Synolakis, C.E., Harkins, G.S., Green, D.R., 1996. Benchmark problem: 2. Runup of solitary waves on a circular island. In: Yeh, H., Liu, P.L., Synolakis, C.E. (Eds.), Long-Wave Run-Up Models. World Scientific, Singapore, pp. 363–374.

Brocchini, M., Peregrine, D.H., 1996. Integral flow properties of the swash zone and averaging. J. Fluid Mech. 317, 241–273.

Brocchini, M., Bernetti, R., Mancinelli, A., Albertini, G., 2001. An efficient solver for nearshore flows based on the WAF method. Coast. Eng. 43, 105–129.

Carrier, G.F., Greenspan, H.P., 1958. Water waves of finite amplitude on a sloping beach. J. Fluid Mech. 4, 97–109.

Coates, T.T., Jones, R.J., Bona, P.F.D., 1998. Wind/swell seas and steep approach slopes, Tech. Rep. TR 24. Hydraulics Research Wallingford.

De Waal, J.P., Van Der Meer, J.W., 1992. Wave runup and overtopping on coastal structures. Proc. 23rd Int. Conf. Coastal Eng. A.S.C.E., Venice, pp. 1758–1771.

Dodd, N., 1998. A numerical model of wave run-up, overtopping and regeneration. ASCE J. Waterw. Port Coast. Ocean Eng. 124 (2), 73–81.

Glaister, P., 1990. Approximate Riemann solutions of the 2-dimensional shallow water equations. J. Eng. Math. 24, 45–53.

Godunov, S.K., 1959. A difference scheme for numerical computations of discontinuous solution of hydrodynamic equations. Math. Sb. 47, 271–306.

Harten, A., Lax, P.D., van Leer, B., 1983. Upstream differencing and Godunov-type schemes for hyperbolic conservation laws. SIAM Rev. 25, 35–61.

Hibberd, S., Peregrine, D.H., 1979. Surf and run-up on a beach: a uniform bore. J. Fluid Mech. 95, 323–345.

Hirsch, C., 1990. Numerical Computation of Internal and External Flows, vol. 2. Wiley, New York.

Hu, K., Mingham, C.G., Causon, D.M., 2000. Numerical simulation of wave overtopping of coastal structures using the non-linear shallow water equations. Coast. Eng. 41, 433–465.

Hubbard, M.E., 1999. Multidimensional slope limiters for MUSCL-type finite volume schemes on unstructured grids. J. Comput. Phys. 155, 54–74.

Hubbard, M.E., Garcia-Navarro, P., 2000. Flux difference splitting and the balancing of source terms and flux gradients. J. Comput. Phys. 165, 1–10.

Kobayashi, N., Watson, K.D., 1987. Wave reflection and runup on smooth slopes. Proc. Coast. Hydrodynamics. A.S.C.E., New York, pp. 548–563.

Kobayashi, N., Otta, A.K., Roy, I., 1987. Wave reflection and run-up on rough slopes. ASCE J. Waterw. Port Coast. Ocean Eng. 113 (3), 282–298.

Kobayashi, N., De Silva, G., Watson, K., 1989. Wave transformation and swash oscillations on gentle and steep slopes. J. Geophys. Res. 94, 951–966.

LeVeque, R.J., 1992. Numerical methods for conservation laws. Lectures in Mathematics, 2nd ed. Birkhäuser, Basel.

Liu, P.L.-F., Cho, Y., Briggs, M.J., Kanoglu, U., Synolakis, C.E., 1995. Runup of solitary waves on circular island. J. Fluid Mech. 302, 259–285.

Manual on the Use of Rock on Coastal and Shoreline Engineering, 1991. Construction Industry Research and Information Association and Centre for Civil Engineering Research and Codes.

Masamura, K., Fuijima, K., 1996. Three-dimensional analysis of long-wave runup on a conical island by using the MAC method. In: Yeh, H., Liu, P.L., Synolakis, C.E. (Eds.), Long-Wave Run-Up Models. World Scientific, Singapore, pp. 321–331.

Owen, M., 1980. Design of seawalls allowing for wave overtopping, Tech. Rep. EX 924. Hydraulics Research Wallingford.

Owen, M.W., 1982. Overtopping of sea defences. Int. Conf. on the Hydraulic Modelling of Civil Eng. Structures. University of Warwick, Coventry, pp. 469–480.

Özkan-Haller, H.T., Kirby, J.T., 1997. A Fourier-Chebyshev collocation method for the shallow water equations including shoreline runup. Appl. Ocean Res. 19, 21–34.

Quirk, J., 1991. An adaptive grid algorithm for computational shock hydrodynamics, PhD thesis, College of Aeronautics. Cranfield Institute of Technology.

Quirk, J.J., Karni, S., 1996. On the dynamics of shock–bubble interaction. J. Fluid Mech. 318, 129–163.

Roe, P.L., 1981. Approximate Riemann solvers, parameter vectors and difference schemes. J. Comput. Phys. 43, 357–372.

Roe, P.L., 1985. Some contributions to the modelling of discontinuous flows. Lect. Appl. Math. 22, 163–193.

Ryrie, S.C., 1983. Longshore motion generated on beaches by obliquely incident bores. J. Fluid Mech. 129, 193–212.

Saville, T., 1955. Laboratory data on wave runup and overtopping on shore structures, Tech. Rep. Tech. Memo. No. 64. U.S. Army, Beach Erosion Board, Document Service Center, Dayton, Ohio.

Shapiro, R., 1970. Smoothing, filtering and boundary effects. Rev. Geophys. 8, 359–387.

Shore Protection Manual, 1984. U.S. Army Corps of Engineers, C.E.R.C. U.S. Government Printing Office, Washington, DC.

Sleigh, P.A., Berzins, M., Gaskell, P.H., Wright, N.G., 1998. An unstructured finite-volume algorithm for predicting flow in rivers and estuaries. Comput. Fluids 27, 479–508.

Takagi, T., 1996. Finite element analysis in benchmark problems 2 and 3. In: Yeh, H., Liu, P.L., Synolakis, C.E. (Eds.), Long-Wave Run-Up Models. World Scientific, Singapore, pp. 258–264.

Takahashi, T., Takahashi, T., Shuto, N., Imamura, F., Ortiz, M., 1995. Source models for the 1993 Hokkaido-Nansei-Oki earthquake tsunami. Pure Appl. Geophys. 144 (3/4), 747–768.

Thacker, W.C., 1981. Some exact solutions to the nonlinear shallow-water wave equations. J. Fluid Mech. 107, 499–508.

Titov, V.V., Synolakis, C.E., 1995. Modeling of breaking and nonbreaking long-wave evolution and runup using VTCS-2. ASCE J. Waterw. Port Coast. Ocean Eng. 121 (6), 308–316.

Titov, V.V., Synolakis, C.E., 1996. Numerical modeling of 3-d long wave runup using vtcs-3. In: Yeh, H., Liu, P.L., Synolakis, C.E. (Eds.), Long-Wave Run-Up Models. World Scientific, Singapore, pp. 242–248.

Titov, V.V., Synolakis, C.E., 1998. Numerical modeling of tidal wave run-up. ASCE J. Waterw. Port Coast. Ocean Eng. 124 (4), 157–171.

Toro, E.F., 1997. Riemann Solvers and Numerical Methods for Fluid Dynamics. Springer, Berlin.

Van Leer, B., 1979. Towards the ultimate conservative difference scheme V. A second order sequel to Godunov's method. J. Comput. Phys. 32, 101–136.

Watson, G., Peregrine, D.H., Toro, E., 1992. Numerical solution of the shallow water equations on a beach using the weighted average flux method. In: Hirsch, C. (Ed.), Computational Fluid Dynamics, vol. 1. Elsevier.

Yeh, H., Liu, P.L., Synolakis, C.E. (Eds.), 1996. Long Wave Run-up Models. World Scientific, Singapore.

Zelt, J.A., 1986. Tsunamis: the response of harbors with sloping boundaries to long wave excitation, Tech. Rep. KH-R-47. California Institute of Technology.